Combining ultrasound and capillary embedded T-junction microfluidic devices to scale up production of narrow sized microbubbles through acoustic fragmentation

Aaqib H. Khan[#], Xinyue Jiang†, Anuj Kaushik[‡], Hari S. Nair[§], Mohan Edirisinghe†, Karla P. Mercado-Shekhar[§], Himanshu Shekhar[‡], and Sameer V. Dalvi[#]*

Chemical Engineering, Indian Institute of Technology Gandhinagar, Palaj, Gandhinagar - 382355, Gujarat, India

† Department of Mechanical Engineering, University College London (UCL), London WC1E 7JE, U.K.

‡ Electrical Engineering, Indian Institute of Technology Gandhinagar, Palaj, Gandhinagar - 382355, Gujarat, India

§ Biological Engineering, Indian Institute of Technology Gandhinagar, Palaj, Gandhinagar - 382355, Gujarat, India

***E-mail: sameervd@iitgn.ac.in; Phone: 091-79-2395 2408**

ABSTRACT: Microbubbles are tiny gas-filled bubbles that have a variety of applications in ultrasound imaging and therapeutic drug delivery. Microbubbles can be synthesized using a number of techniques including sonication, amalgamation, and saline shaking. These approaches can produce highly concentrated microbubble suspension but offer minimal control over size and polydispersity of microbubbles. One of the simplest and effective method for producing monodisperse microbubbles is capillary embedded T-junctions microfluidic devices which offers great control over microbubble size. However, lower production rates (~200 bubbles/s) and large microbubble sizes (~ 300 µm) limits the applicability of such devices for biomedical applications. To overcome the limitation of these technologies, we demonstrate in this work, an alternative approach to combine capillary embedded T-junction device with ultrasound to enhance generation of narrow sized microbubbles in aqueous suspensions. Two T-junction microfluidic devices were connected in parallel and combined with an ultrasonic horn to produce lipid coated SF_6 core microbubbles in the size range of 1-8 µm. The rate of microbubble production was found to increase from 180 microbubbles/s in absence of ultrasound to $(6.5 \pm 1.2) \times 10^6$ bubble/s in presence of ultrasound (100 % ultrasound amplitude). When stored in a closed environment, the microbubbles were observed to be stable for up to 30 days, with the concentration of the microbubble suspension decreasing

from ~ 2.81 × 10^9/mL to ~ 2.3 × 10^6/mL and size changing from 1.73 ± 0.2 µm to 1.45 ± 0.3 µm at the end of 30 days. The acoustic response of these microbubbles was examined using broadband attenuation spectroscopy, and flow phantom imaging was performed to determine the ability of these microbubble suspensions to enhance contrast relative to the surrounding tissue. Overall, this approach of coupling ultrasound with microfluidic parallelization enabled continuous production of stable microbubbles at high production rates and low polydispersity using simple T-junction devices.

Keywords: Microbubbles; microfluidics; acoustic fragmentation; sonication, dissolution, stability

INTRODUCTION: Microbubbles are gas-filled particles stabilized by a protective shell consisting of lipids[1, 2], proteins[3-5], and polymers[6, 7]. Microbubbles are employed for ultrasound imaging because of their compressible gas core, which allows them to contract and expand in response to an ultrasonic field and generate significantly stronger harmonic echoes than the surrounding tissues[8-11]. The size distribution of the microbubble suspension is of utmost importance in ultrasound contrast imaging and drug delivery. A monodisperse microbubble suspension has been shown to enhance the average scattering cross-section per bubble by nearly two orders of magnitude when compared to a polydisperse microbubble suspension[12]. The use of monodisperse microbubble suspension results in similar resonance frequency and destructive thresholds for effective imaging and drug delivery[13-18]. Commercially approved microbubbles, such as Sonovue, Definity and Optison are usually 1- 5 µm in size and possess low polydispersity index[9, 19]. However, intravenous injection of microbubbles > 8 µm can potentially embolize the microcirculation of the lung[20].

Different approaches have been reported in the literature to produce microbubbles, viz., sonication[21, 22], amalgamation, electrohydrodynamics forming[23], pressurised gyration[24] and microfluidic devices[25]. Sonication and amalgamation can produce highly concentrated microbubbles in a short period, but the size distribution of these microbubble suspensions can be highly polydisperse (1-50 µm), hence these techniques require lengthy size isolation steps to produce narrow sized microbubble suspension[26]. Researchers[27, 28] have used flow-focusing devices to produce narrow-sized microbubble suspensions at production rates of ~ 4×10^5 microbubbles/s. The capillary sizes used were usually 50 µm with the converging nozzle of size ~ 5 µm and the working pressure of 1.1- 1.2 bar (gauge pressure). However, there are reports[29] which show that the use of small channel sizes impose challenges of high gas pressure drop and channel blockages during multiple and long operations of the devices. Very recently, while this work was underway, Carugo et. al.[30] reported a combination of T-junction microfluidic chip with a rectangular geometry and ultrasound to produce a narrow-sized microbubble suspension at a production rate of 10^6 microbubbles/s. The ultrasound exposure time for microbubble fragmentation was only 1s. To increase the production rates the authors use a 500 µm capillary and report production rates upto 10^8 bubbles/s.

However, the use of a coarser capillary led to increase in the polydispersity of the final suspension. The process of microbubble production and long term stability of these microbubbles produced using microbubble fragmentation was missing in the work reported by Carugo et.al. Chen et al.[31] have used sonication-microfluidic devices for the synthesis of microbubbles stabilized by ethyl cellulose nanoparticles. Nanoparticle-coated microbubbles were produced from a large precursor slug bubble by the cavitation process. During cavitation, Faraday waves were observed to generate, which lead to detachment of microbubbles from the large slug bubble. The microbubbles produced after the sonication process were in the size range of 30-40 µm. Microfluidic devices can produce highly monodisperse microbubbles, however, the utility of microfluidic devices, especially the capillary embedded T-junction, is limited due to the lower yield[32-35]. T-junction microfluidics in conjugation with electrohydrodynamics focusing[36-38] has been shown to produce microbubbles of sizes less than 50 µm, but the rate of microbubble production are low.

Therefore, in this work, we present an alternative approach of using two capillary embedded T-junction microfluidic devices connected in parallel along with ultrasound (40s OFF 20s ON) to produce narrow-sized microbubble of sizes < 8 µm continuously by acoustic fragmentation process. We capture the in-situ acoustic fragmentation process in micro capillaries of sizes 65, 100 and 200 µm using a high-speed camera operated at 50000 - 100000 frames/s. We utilise a custom image processing Matlab code to process the microbubble evolution in presence of ultrasound. The shelf stability and the dissolution behaviour of the microbubbles prepared using sonication alone and microfluidic combined with sonication in an air-saturated environment was also investigated. Finally, we conduct broadband attenuation, and flow phantom studies for acoustic characterization of the microbubbles.

METHODS AND MATERIALS

Materials: 1,2-distearoyl-sn-glycero-3-phosphocholine (DSPC) (Avanti Polar Lipids, India) and poly (ethylene glycol) 40 (PEG40) stearate was obtained from Sigma-Aldrich India. These were used without further

purification. Sulphur Hexafluoride (SF_6) (Ultrahigh pure grade), used as a dispersed phase during microbubble preparation, was purchased from JP gas suppliers India.

Solution preparation: Lipid solution was prepared in molar ratio of (9:1) to a final concentration 2 mg/mL, 5mg/mL and 10 mg/mL as described in earlier reports[39]. Briefly, 1,2-distearoyl-sn-glycero-3-phosphocholine (DSPC) and poly (ethylene glycol) 40 (PEG40) stearate was dissolved in chloroform. Chloroform from DSPC PEG 40S mixture was allowed to evaporate overnight. PBS was added to the dried DSPC-PEG40S film and heated to 65℃ followed by sonicating the solution at 30 % amplitude using a 500 W sonicator (Sonics, Vibra cell) and cooled immediately using ice bath maintained at ~ 4-5 ℃. PBS used in the experiment was vacuumed overnight and saturated with SF_6 gas.

Experimental setup: The experimental setup (Figure 1) consisted of a cross-flow type microfluidic T- junction made of a Polymethyl methacrylate (PMMA, Direct Plastic Ltd., United Kingdom) block of dimension (10 × 10 × 20 mm^3), which consisted of 1.6 mm hollow channels. Teflon Fluorinated Ethylene Polypropylene (TFEP) capillaries with outer diameter of 1.6 mm and inner diameters of 200, 100 and 65 µm were inserted into the PMMA block for three separate studies. High-grade HPLC fittings were used to connect capillaries to the PMMA block to avoid fluid leakage. A subsequent third capillary of the same diameter was placed into the PMMA block, perpendicularly oriented to other capillaries to develop the cross-flow. The outlet capillary of the T-junction was passed through a "sonication well" such that the outlet capillary is supported by the bottom of the sonication well. The sonicator probe was inserted into the sonication well allowing the sonicator tip to contact the capillary tube directly. The sonication well was filled with cold water at ~5℃. Fig. 1 depicts the assembled schematic representation of the experimental setup. The top capillary of the T-junction was connected to a gas-regulator connected to the SF_6 gas cylinder. The inlet gas pressure was monitored using a digital pressure gauge (EN-400, purchased from Adarsh Industries, Mumbai-India). Aqueous phase was injected into the T-junction using a Harvard syringe pump (PHD ultra-infusion only), to allow non-pulsating liquid flow. Two T-junctions were connected in parallel to double the production rate of the microbubble formation.

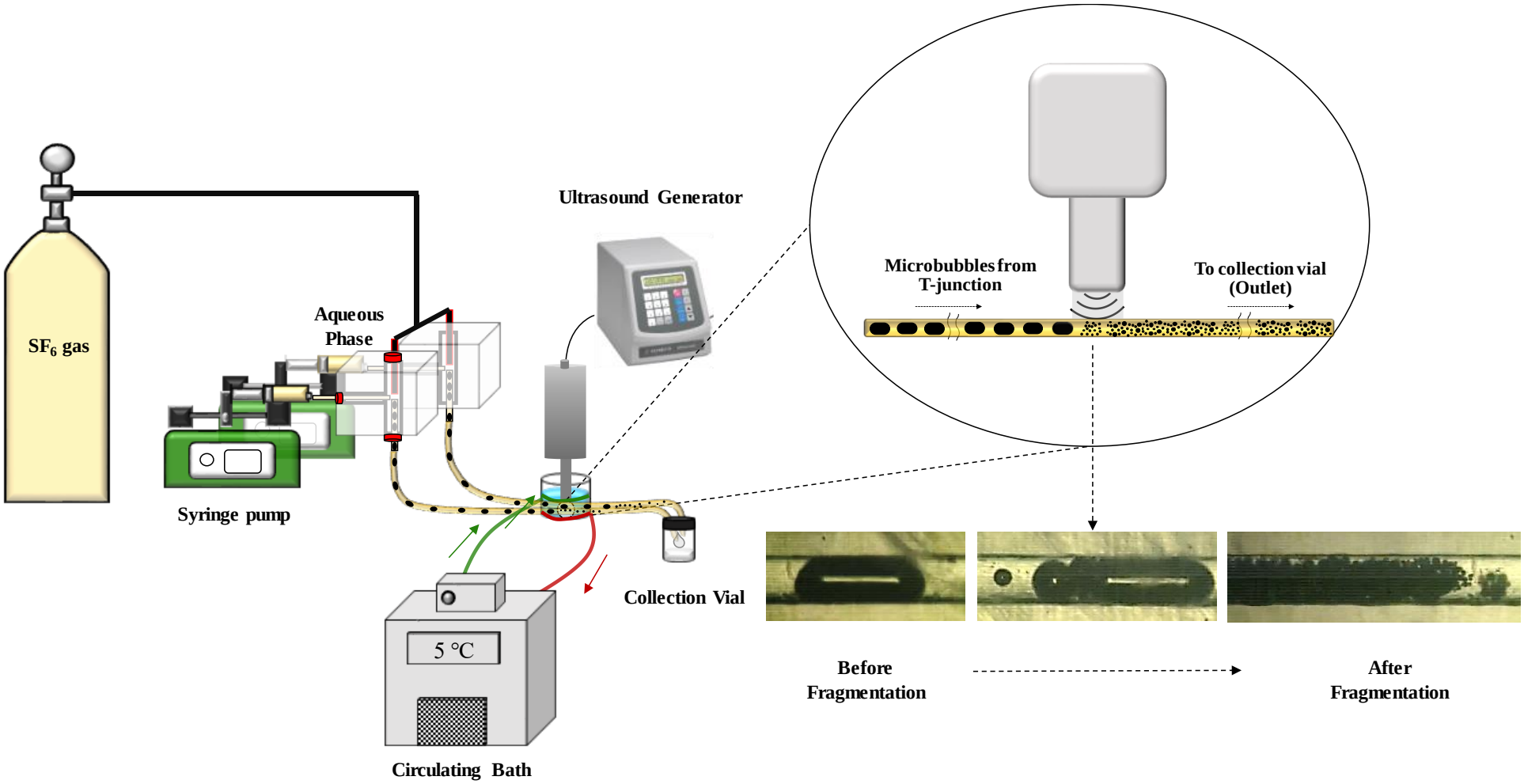

Figure 1. Schematic of experimental setup for microbubble generation using combined sonication and microfluidics. SF_6 as the gaseous core is supplied to two T-junction microfluidic devices connected in parallel with the extend outlet capillary coupled with a probe sonicator in a sonication well. Temperature of the sonication was maintained at ~ 5 °C.

The outlet of the T-junctions was inserted into a 10 mL crimped vial to collect the fresh microbubble suspension in a closed environment. A 21G needle was inserted into the vial to prevent pressure build up. Collection of microbubbles in a closed environment significantly improved the stability of microbubbles. Freshly prepared microbubbles were separated and stored in 2 ml crimped vials with the head space replaced with SF_6 for optical imaging and further size characterization.

Shelf stability and *in-vitro* dissolution stability of microbubbles: Size isolated microbubbles were collected in vials and stored at 4 ℃ in air tight condition in 2 ml crimped vials. At definite time intervals, 2 µL of microbubble suspension was inserted to the Particle Sizing Systems (Accusizer 780AD, NICOMP) and the size distribution was recorded. A custom-made dissolution chamber made of acrylic was used to observe the *in-vitro* behaviour of microbubble dissolution. The dissolution behaviour of microbubbles with a diameter of ~ 6-8 µm was observed under an optical microscope at magnification of 40X and 60 X and recorded until the complete dissolution of microbubbles.

Rate of microbubble production:

Microbubble production rate in microfluidic device was determined using the concentration of the microbubble suspension obtained from Accusizer 780AD, NICOMP Particle Sizing Systems as indicated by equation (1).

$$\text{Bubble production rate (microbubbles/s)} = \frac{\text{Microbubble Concentration/mL}}{\text{Total collection time (s)}} \times \text{Volume of the MB suspension (mL)} \qquad (1)$$

Image analysis of evolution of the microbubble in the microfluidic capillary: To characterise the shape irregularities of the rectangular oval gas slug appeared due to ultrasound exposure, the slug's contour was tracked using image analysis routines in Matlab (v. 2019b, Mathworks, USA)., as described by Poulichet et. al[40]. The image analysis involves two steps, first a black and white threshold is applied to the snapshot using an inbuilt function *imbinarize*, following which the edges of the gas slug are tracked using the function *bwboundary*, and the boundary-pixels coordinates are saved.

The centroid of the gas slug was determined using function *regionprops*. The distance between the boundary coordinates and the centroid was then estimated [A (t, θ_c)], following which three reference points were chosen

to measure the slug length as shown in Fig. S1, (i) centre of the slug (marked as 2 in Fig. S1), (ii & iii) the farthest points on the x-axis of the slug (marked as 1 and 3 in Fig. S1). The microbubble fragmentation process was captured at 50000 - 100000 frames/s using a Photron High speed camera (Fastcam MINI UX 100) with 10 µm pixel pitch. Fragmenting location of the microbubble interface was located first from the high-speed video clips, and the location was tracked backward by keeping the ratio x_1/x_2 constant to measure the change in radial slug length with time.

Table1. Stable operating conditions for a single T-junction device for different micro capillaries

Capillary Size (µm)	Liquid Flow rate (ml/min)	Gas pressure (bar)	Average microbubble size (µm)
200	0.3	0.2	260
100	0.1	0.8	110
65	0.075	1.4	40

Broadband attenuation spectroscopy measurements

Figure S2 depicts the schematic of the broadband attenuation spectroscopy setup. All acoustic studies were conducted in a 22 L plexiglass water tank with dimensions of (20×10×10 in.). The through-transmission spectrum was obtained using a broadband pulse excitation using two polyvinylidene fluoride (PVDF) transducers (Precision Acoustics, Dorchester UK). The focal length, aperture diameter, and center frequency of these transducers were 40 mm, 6 mm, and 20 MHz, respectively[41, 42]. An ultrasonic pulser receiver (JSR DPR300, DA1366, Imaginant Inc., Pittsford, NY 14534) was used to create the excitation pulse with a pulse repetition frequency of 100 Hz. The transmitted pulse amplitude was controlled by an inline variable attenuator (RITEC Model RA-32, Ritec Inc., Warwick, RI, USA). A 0.2 mm needle hydrophone (Precision Acoustics, Dorchester, Dorset, UK) was used to calibrate the acoustic pressure at the focus. A peak rarefactional pressure of 34 kPA was used to avoid nonlinear propagation. The average of 128 received waveforms was digitized with an oscilloscope (Tektronix MD03014; 8 bits, 2.5 GHz sampling rate, 100 MHz bandwidth, Tektronix Inc., USA) and then downloaded to a personal

computer for analysis using MATLAB (v. 2019b, Mathworks, USA). The sample chamber with acoustically transparent windows was positioned between the two PVDF transducers (see Fig. S2).

Frequency dependent attenuation coefficient, $\alpha(f)$ (in dB/cm), was calculated using a broadband substitution technique[43]. The attenuation coefficient was determined (Equation 2) using the measured voltage time waveform. The route length which the ultrasonic waves communicates with the UCA suspension is d (2.6 mm). And, the amplitude spectra obtained for DI water with and without microbubble suspension are V_{sample} and V_{ref}, respectively. Attenuation was measured across a frequency range of 2 MHz to 25 MHz, corresponding to a –20 dB bandwidth system using the following equation:

$$\alpha_{meas}(f) = 10\log_{10}\left(\frac{|V_{ref}(f)|^2}{|V_{sample}(f)|^2}\right)/d \quad (2)$$

Estimation of shell properties

The viscoelastic shell properties were measured using the De Jong model[44]. The properties which characterize the microbubble shell are (i) shell elasticity (S_P) and (ii) shell friction (S_F). According to the Marmottant model in the linear regime, the shell elasticity and friction are expressed as, $S_P = 2\chi$ and $S_F = 16\pi\kappa_S$,[45] where χ is the elastic modulus and κ_S is the dilatational viscosity (depends on bulk lipid viscosity, μ_{lipid}) . The viscoelastic parameters were estimated by minimizing the sum squared error between the observed and the predicted attenuation coefficient, assuming linear scattering. The quality of fit between the experimental and predicted attenuation coefficient was determined using coefficient of determination (R^2).

In vitro B-mode imaging of microbubbles in tissue-mimicking flow phantoms

A tissue-mimicking phantom was developed using previous standardized protocols.[46] The phantom was made of 10 %(w/v) poly(vinyl alcohol) (PVA) (Elvanol® 71-30, Houston, TX, U.S.A.) and 2 %(w/v) silicon carbide particles (400 mesh, Sigma Aldrich, Buenos Aires, Argentina) with a 5 mm diameter flow channel. Silicone tubes of diameter 5 mm were used to link the two ends of the phantom flow channels. Freshly synthesized microbubbles of mean diameters 1-3 µm were diluted to 10^5, 10^6, and 10^7 microbubbles/mL using DI water. The diluted microbubble suspension was gently introduced into the flow phantom using a syringe pump (S750i, Omya

Healthcare, Bengaluru, India). The phantom flow channel was filled with Milli-Q or DI water before inserting the diluted microbubble solution (Fig S3) to observe a clear change in contrast due to the presence of microbubbles. A programmable research ultrasound system (Vantage 128, Verasonics, Inc., Kirkland, WA, USA) equipped with a L11-5v linear array transducer was used to perform the flow phantom imaging. Fig. S3 depicts the schematic of the imaging setup. The L11-5v linear array transducer had a center frequency of 7.6 MHz. The backscattered signal was quantized at a 14-bit resolution and sampled at 30.4 MHz. MATLAB (v. 2019b) was used to post-process the image data.

Two regions of interest (ROI) were selected in each B-mode image: 1) ROI located in the flow channel region containing the microbubble suspension, and 2) ROI outside the flow channel. Subsequently, the Contrast to Noise ratio (CNR) and Contrast to Tissue (phantom) ratio (CTR) were calculated for three ROI pairs in each B-mode frame to assess the imaging quality[47, 48] (Fig. S4). The expressions for CNR and CTR calculation are as follows:

$$\mathrm{CTR} = 20\log_{10}\frac{Mean\ pixel\ intensity\ of\ microbubble\ filled\ channel\ region}{\text{Mean pixel intensity of phantom region}} \quad (3)$$

$$\mathrm{CNR} = 20\log_{10}\frac{\frac{Mean\ pixel\ intensity\ of\ microbubble\ filled\ channel\ region}{\text{Mean pixel intensity of phantom region}}}{\text{standard deviation of pixel intensity of phantom region}} \quad (4)$$

Results and Discussion

Generation of microbubbles in T-junction microfluidic device combined with sonication

Table 1 presents the operating conditions for single T-junction devices embedded with different sizes of micro-capillaries. It is evident from Table 1 that a decrease in capillary size reduced the flow rate of the aqueous phase but increased the gas pressure to maintain a stable flow. The increase in gas pressure is a consequence of increased flow resistance experienced by the liquid and gas phase due to the reduction in flow cross-sectional area. For all experiments, the T-junctions were allowed to run for at least 5 minutes to achieve a stable flow conducive to microbubble formation. Following which, the microfluidic capillary coming out of T-junctions was coupled with the sonicator probe in a beaker consisting of cold water. The distance between the sonicator probe and the microfluidic capillary was vital for microbubble fragmentation (See Video S1, S2, S3). It can be observed from video S3 that microbubbles undergo fragmentation only when the probe is in direct physical contact with the

micro-capillaries. The conjugation of ultrasound to micro-capillaries introduced intense acoustic vibration that assisted fragmentation of large gas slug into daughter slugs. Therefore, all fragmentation experiments were performed with the sonicator probe in direct proximity of micro-capillaries.

Figure 2 presents snapshots of the sequence of microbubble fragmentation process captured at 10^5 fps. It can be observed from Fig. 2 that the onset of ultrasound exposure introduces surface instabilities which continuously deforms the gas slug. The gas slug was observed to compress (t = 0 μs) in the direction of ultrasound during the high pressure cycles, while expand and retract back (t = 30 μs) to the original rectangular oval shape during the low pressure cycle. Unlike a free microbubble oscillation in presence of ultrasound[49], the oscillation of a bounded gas slug was significantly affected due to the presence of wall in a close vicinity[50]. The behavior of microbubble oscillation in the capillary tube observed in this work matches with the previous observation by Thomas et. al.[51], where the authors reported that the amplitude of oscillation of a 10 μm microbubble decreases by 50% in a 25 μm capillary tube as compared to a 10 μm microbubble oscillating in a larger, 160 μm capillary tube, due to the presence of rigid wall.

In Fig. 2, after 180 μs, the gas slug can be observed to form a crown shaped slug, due to formation of alternating crest and trough, and elongate axially during the compression cycle. Wu et al.[52] reported similar behavior for a 40 μm size microbubble oscillating near a rigid wall. The authors reported that upon striking the wall, the microbubble elongates axially, forming an ellipsoidal shape followed by formation of an inward micro-jet that ultimately impales the microbubble leading to fragmentation. As shown in Fig. 2, the oscillation of the gas slug after 630 μs was observed to become violent, leading to jetting of small bubbles from the slug surface (t = 680 μs), possibly due to formation of nonlinear standing waves at the gas–liquid interface[31, 53]. The jetting of microbubbles from the gas-liquid interface was more pronounced for larger microbubbles (see Video S5, S6). After 690 μs, micro-jets were observed to form which ultimately pierced the gas slug into daughter slugs. The daughter slugs were observed to further fragment into even smaller slugs in a similar fashion and produce a cluster of narrow sized microbubble suspension as can be seen from Fig. 2 (after 990 s).

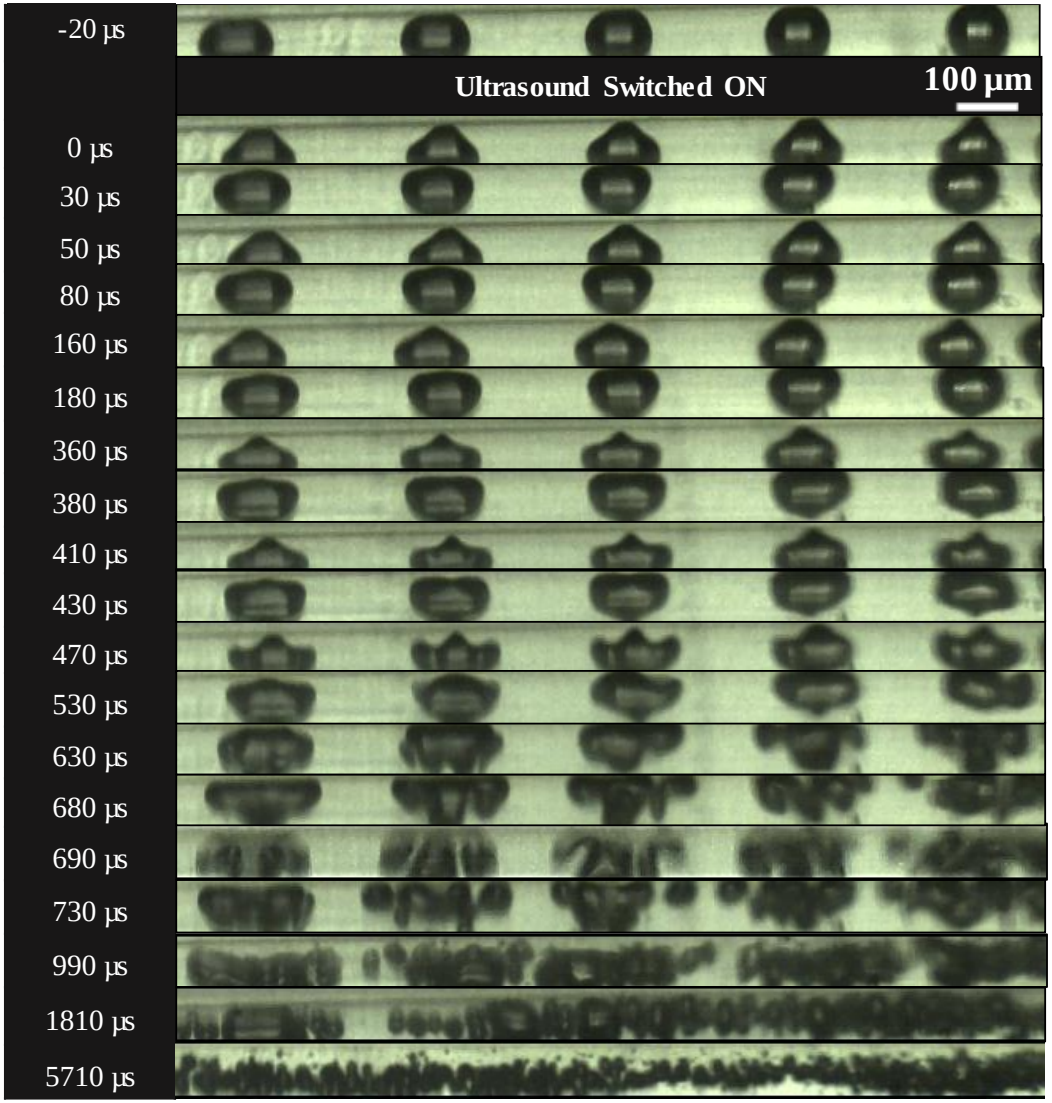

Figure 2. Snapshots of high speed video clips of microbubble fragmentation process recorded at 100000 frames/s. The diameter of the micro-capillary is 100 µm, and the ultrasound amplitude is 100 %. Negative time indicates the image frame before the onset of ultrasound.

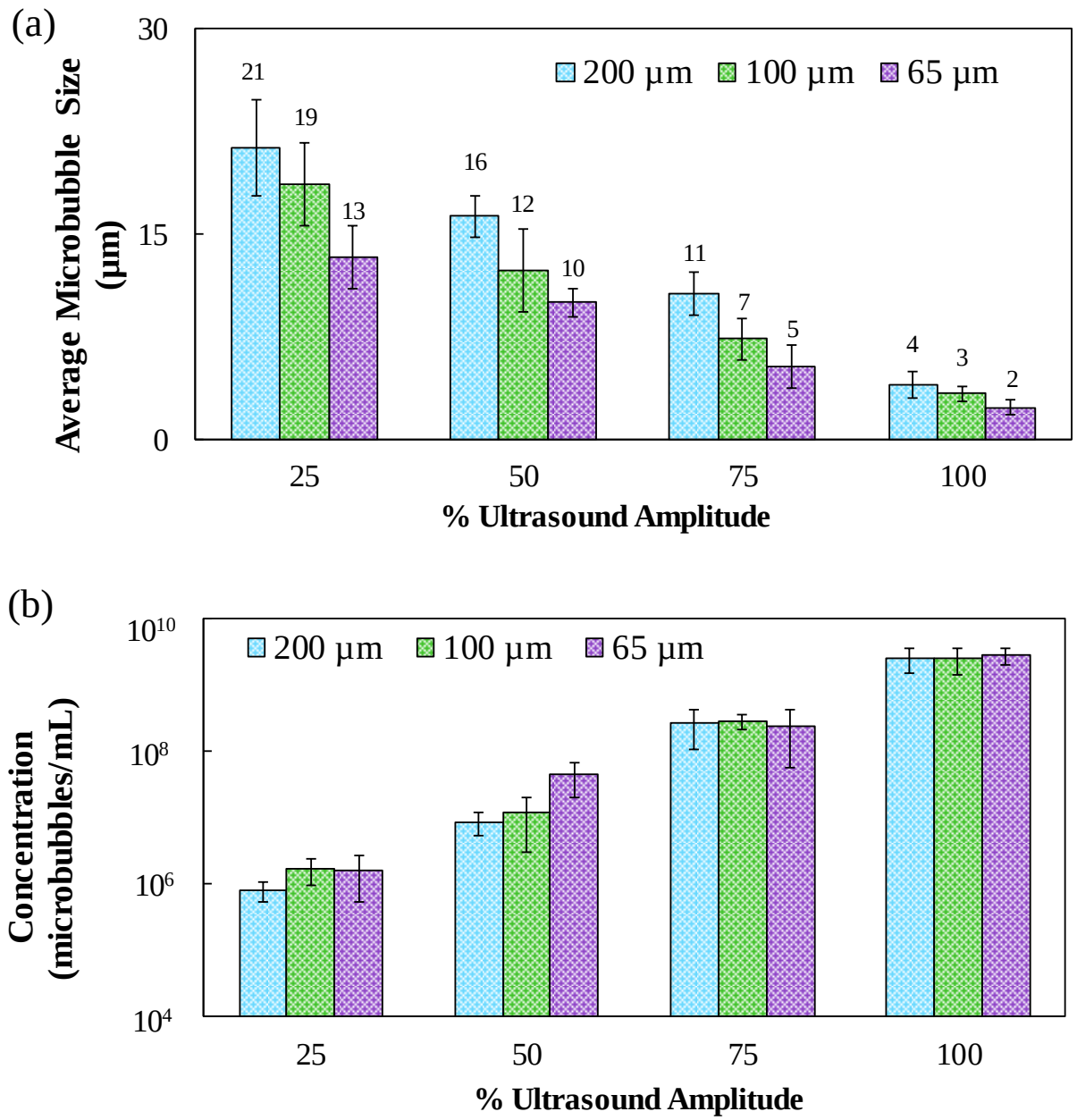

Figure 3. Effect of ultrasound intensity and capillary size on (a) average size and (b) concentration of the fragmented microbubble suspension

Fig. 3 presents the effect of ultrasonic amplitude on the average size (Fig. 3a) and the concentration (Fig.3b) of microbubbles in aqueous suspension. It can be observed that with an increase in ultrasound amplitude from 25 % to 100 %, the microbubble size decreased for all three capillary sizes. The lowest microbubble sizes of 4 ± 1.7, 3 ± 1.5, 2 ± 1 µm were obtained for capillary size of 200, 100 and 65 µm, respectively at 100 % ultrasound intensity

(Fig. 3a). With an increase in intensity from 0 to 100 % the concentration of the microbubble suspension increased from (8.4 ± 2.6) $\times 10^5$ to (2.6 ± 1) $\times 10^9$ for 200 µm capillary, from (1.57± 0.7) $\times 10^6$ to (2.56 ± 1.2) $\times 10^9$ for 100 µm capillary, and from (1.6 ± 1.05) $\times 10^6$ to (2.74 ± 0.8) $\times 10^9$ for 65 µm capillary. This indicates that an increase in the ultrasonic power increases the concentration of microbubbles and decreases the microbubble size.

These observations are consistent with the previous study by Chen et. al[31] , where the concentration of microbubbles was reported to increase with the increase in ultrasonic power from 50 W to 600 W due to higher cavitation of the slug bubbles.

Compared to 65 and 100 µm capillaries, 200 µm capillary provides larger gas slugs for microbubble fragmentation due to a large channel size. Further, it requires gentle flow parameters for smooth and stable microfluidic operation. Therefore, 200 µm capillary tubing was used in this work for large scale production of narrow sized microbubble suspensions. Two T-junctions with a capillary size of 200 µm were then operated simultaneously at the same flowrate with the probe sonicator operated in the pulse mode of 40s ON and 20s OFF cycles. DI water in the sonication well was maintained at 5 °C using a circulating bath to avoid overheating of the sonicator tip touching the capillary tube. Fragmented microbubbles were collected in a closed environment and separated from the large foam bubbles in a separate vial to avoid Ostwald ripening.

The fresh microbubble suspension, was analysed for size distribution and concentration using Accusizer 780AD, NICOMP Particle Sizing Systems, Santa Barbara, CA. The concentration of microbubbles was observed to increase from ~10^6 bubbles/mL at 25% amplitude to ~10^9 bubbles/mL at 100 % amplitude (Fig. 3b). Fig. 4 (a-d) present the size distribution of the microbubble suspension obtained using and 200 µm capillary at varying ultrasound amplitude (0 to 100 %). In the absence of ultrasound large microbubbles in size range of 260 ± 4.2 µm are obtained (Fig. S5). However, increasing the ultrasonic amplitude from 25% (Fig. 4a) to 100% (Fig. 4d) reduced the size of microbubbles owing to fragmentation and also decreased the polydispersity of the microbubble suspension. As shown in Fig. 4, the peaks at 4-6 µm and larger size ranges in the number and volume-weighted distribution were observed to decrease with an increase in the ultrasound amplitude.

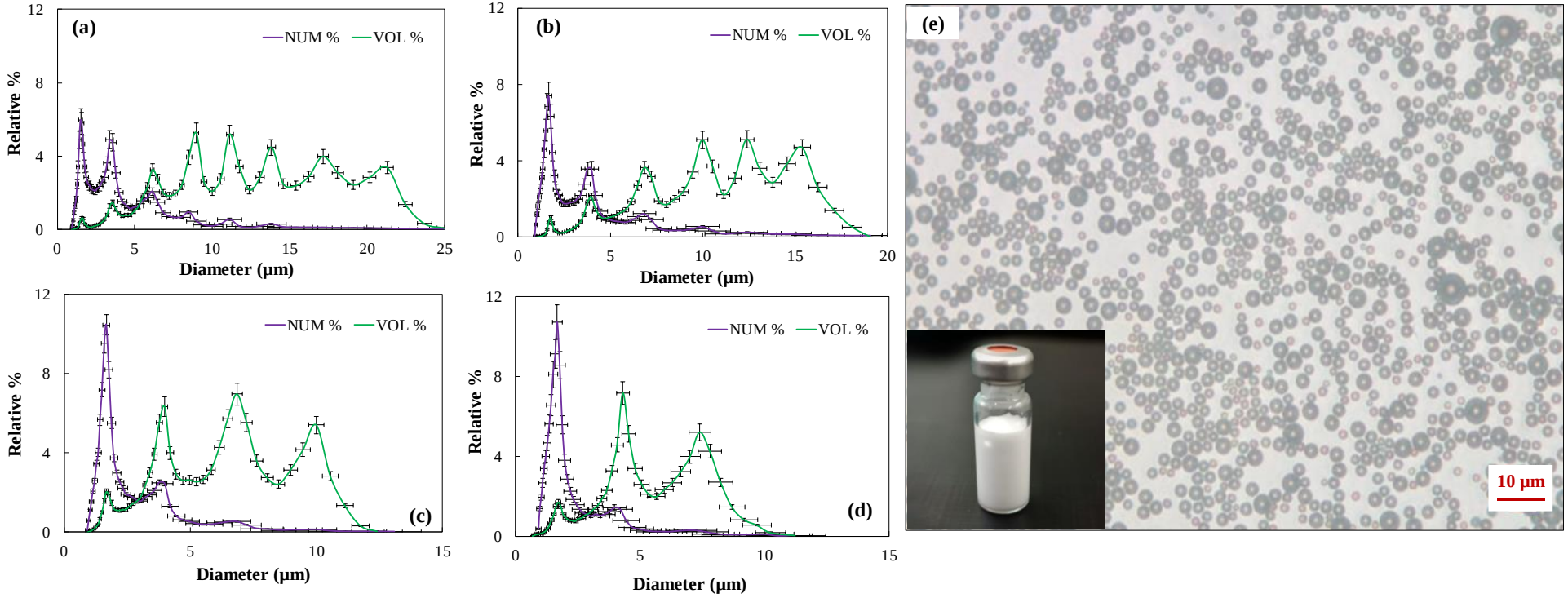

Figure 4. (a-d) Effect of ultrasound intensity on the size distribution of the fragmented microbubble suspension for a 200 µm capillary operated at 0.3 ml/min aqueous flowrate and 0.2 bar pressure (a) 25% ultrasound amplitude (b) 50% ultrasound amplitude (c) 75% ultrasound amplitude (d) 100% ultrasound amplitude (e) Optical image of the fresh microbubble suspension obtained at 100 % amplitude. Inset shows the image of glass the vial containing fresh microbubble suspension.

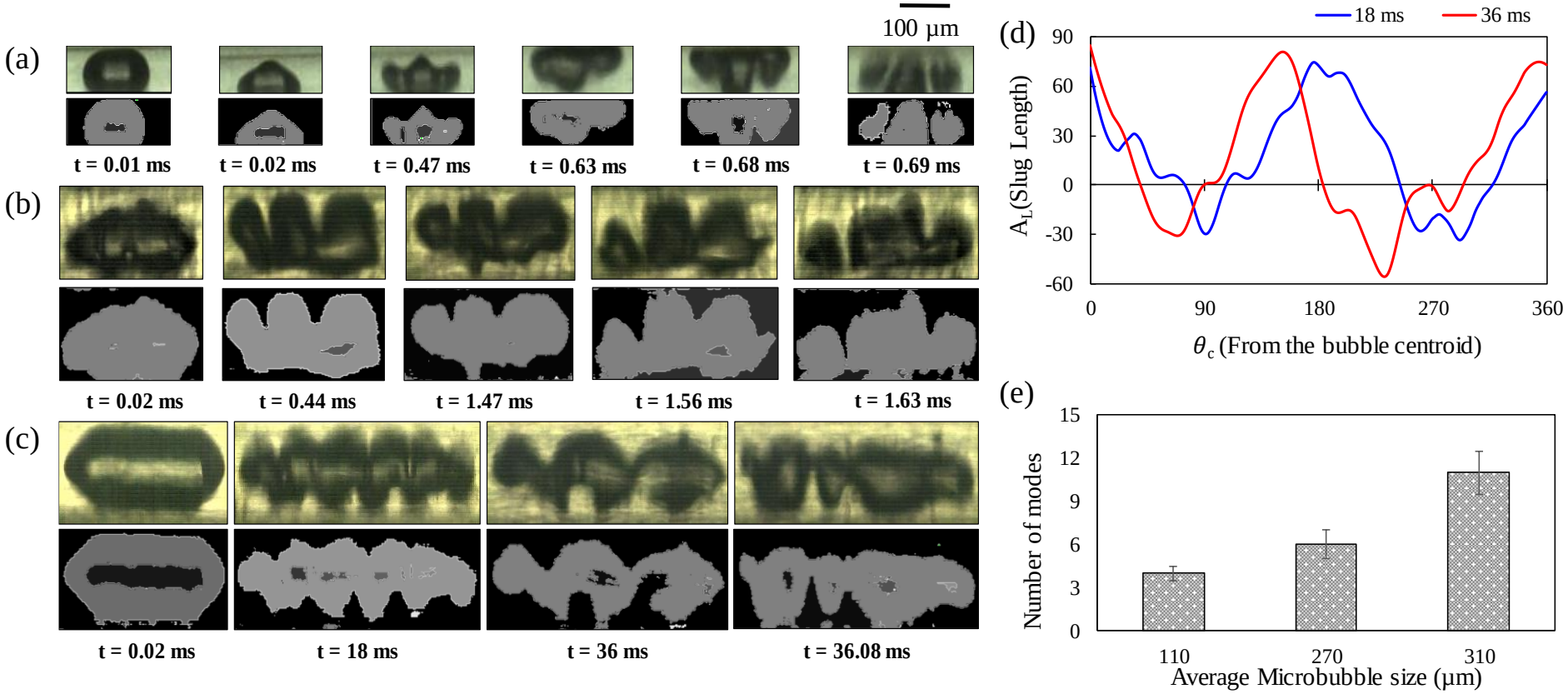

Figure 5. Snapshots of high speed imaging highlighting the shape oscillation of microbubbles insonified at an ultrasound frequency of 20kHz (a, b, c) and their boundary trace (d) Departure of a 310 µm gas slug from initial rectangular oval shape, obtained by subtracting instantaneous slug length (t = 0) and slug length at time t = 0.02 ms (e) Maximum number of surface modes of oscillation for different microbubble size.

This suggests that an increase in the ultrasound amplitude leads to formation of a narrow-sized microbubble population with higher contents of microbubbles in 1-3 μm size range.

It can also be observed from Fig. 4d that the microbubble suspension produced at 100 % ultrasonic intensity consists of microbubbles in the size range of 1-8 μm with peaks at 1-3 and 4-8 μm. Though the number population of larger microbubbles were less, as presented by the number weighted distribution in Fig 4d, the volume occupied by these bubbles was high (as shown by the volume-weighted distribution). The presence of microbubbles of larger sizes can result in inter-bubble gas exchange due to the pressure gradient between large and small bubbles. Therefore, the fresh microbubble suspension was size isolated to produce suspension containing (1-3 μm) from the large bubbles (4-8 μm) by centrifuging the suspension at 90g for 1 min. Freshly prepared microbubble suspension containing microbubbles in the size range of 1-3 μm was stored in air-tight condition with the headspace replaced with SF_6 gas (Inset of Fig. 4e).

Microbubble fragmentation in presence of ultrasound

Temporal evolution of bounded gas slug in presence of ultrasound

In this work, gas slugs were excited at an ultrasound frequency of 20 kHz with the acoustic pressure oscillating in time with a period of T = 1/f = 0.05 ms. In response to alternating pressure field, the microbubbles were observed to undergo shape oscillation before fragmentation. Fig. 5 (a-c) presents a series of snapshots of high-speed videos presenting shape oscillation of a 110, 270 & 310 μm gas slugs and their corresponding boundary trace at different times before fragmentation. Using image analysis routines in Matlab presented in Section 2.7, the boundary of the gas slug was traced, and the pixel coordinates of the traced boundary were utilized to measure the radius and lateral length of the gas slug.

Fig. 5d presents the deviation in the shape of the 310 μm gas slug from the initial rectangular oval gas slug (t = 0.02 ms) upon exposure to ultrasound. Variation in slug length [A (t, θ_c)] with θ_c (varying from 0 to 2π, angle from the centroid) was found by measuring the distance between the centroid and coordinates on the slug boundary. The variation in slug length for subsequent times during the ultrasound exposure was found by

following the same Matlab routine and were subtracted from in the initial slug length, to measure the change in slug length $\Delta A = A(t, \theta_c) - A(t_0, \theta_c)$, which helped to quantify the number of surface modes. The maximum number of surface modes for three different sizes of gas slug in presented in Fig. 5e. The number of surface modes was observed to increase with the increase in the size of the gas slug. The surface modes were observed to be 11±2 for the large gas slugs as compared to 3±1 for the smallest gas slug.

Variation in radial and axial length of the gas slug in presence of ultrasound: Fig. 6a presents the change in the axial and radial slug lengths of a confined gas slug. Unlike a spherical gas slug[49], the length of the rectangular-oval gas slug differs in radial and axial directions, hence three reference points were chosen to characterize the gas slug, which are the centroid of the gas slug and the two farthest points on the major and the minor axis of the gas slug shown in Fig S1. The change in the axial and radial lengths in Fig 6a was plotted from high-speed video snapshots presented in Fig.2 for microbubble fragmentation at 100% for every 10 μs. The gas slug was observed to follow three stages; oscillation, slug elongation, and fragmentation. During the first stage of the oscillation, the radial and axial length of the gas slug was observed to decrease and increase, respectively, immediately after the ultrasound was switched ON. The gas slug oscillated with increasing number of modes (Fig 5e) with continuous elongation in the micro-capillary. For a microbubble oscillating near a wall, at high acoustic excitations, the microbubble implodes after a few acoustic cycles and generates a high velocity fluid jet, due to fluid inertia, directed towards the wall which leads to microbubble fragmentation[11, 54-58]. Apart from micro-jet formation, Laplace pressure gradient induced due to necking of the gas slug may also contribute to gas slug fragmentation[59]. As the re-entrant jet squeezes the gas slug to form a neck during the fragmentation process, the Laplace pressure near the neck region increases due to smaller curvature than the rest of the gas slug. Therefore, the Laplace pressure gradient makes the fluid flow to the location of lower Laplace pressure and fragments the gas slug. In addition to the volumetric oscillation of the gas slug, we observed that the vibration introduced in the micro-capillary due to the transfer of momentum by the translation motion of the sonicator tip to the micro-capillary led to multiple rebounds of the gas slug (see Video S4, S5, S6). Therefore, a combined effect of volumetric oscillation

and rebounds of the gas slug in the micro-capillary leads to the generation of narrow-sized microbubble suspension.

The change in radial and axial lengths at lower ultrasound amplitudes are presented in Fig. S6-S8. It can be observed that when the ultrasonic amplitude was reduced, the time for the onset of microbubble fragmentation increased from 1050 s for 100% amplitude to 3020 s for 25% amplitude. The velocity of the microbubble interface decreased from ~ 6 m/s for 100 % amplitude to ~ 4-5 m/s for 25 % amplitude. Decrease in the time for fragmentation and increase in the interface velocity with the increase in ultrasound amplitude suggests that microbubble fragmentation was quicker and better at higher ultrasound amplitude.

Fragmented gas slugs may also coalesce during mutual interaction between microbubbles in the presence of ultrasound. The interaction between microbubbles due to secondary ultrasound fields emitted by the neighbouring microbubbles are explained by secondary Bjerknes forces[60], where microbubbles may repel or attract each other depending upon the driving frequency. Microbubbles may repel each other if the driving frequency lies between the resonance frequency of interacting microbubbles otherwise the microbubbles may experience attractive forces[61]. The resonance size of the microbubble driven at 20 kHz frequency is ~ 163 μm[62]. Therefore, microbubbles of sizes except for above or below 163 μm may experience repulsive forces. Also, in this work we have used DSPC-PEG40S in the continuous phase solution to produce microbubbles which possibly restricts excessive coalescence of microbubbles due to electrostatic and steric stabilization[63, 64].

Velocity characteristics of microbubble during fragmentation: To further investigate the characteristics of acoustic microbubble fragmentation, the velocity profile of the points on the microbubble surface undergoing fragmentation was measured with reference to the centroid and the farthest points of the microbubble. Fig. 6b presents the change in the crest length of the fragmenting location tracked backwards during the microbubble fragmentation process. The velocity (v) was estimated by making a difference in the crest length divided by the time intervals between two adjacent frames.

Fig. 6c presents the velocity profile of the fragmenting location on the microbubble interface with time until the first fragmentation. The microbubble fragmentation process comprised of three stages: oscillation, slug elongation, and fragmentation. The increase in the velocity initially corresponds to the onset of oscillation of the gas slug in response to ultrasound. Following which velocities increase gradually during the slug elongation phase and become nearly constant thereafter. During the final stages, a spike in the velocity profile was observed, during which the velocity was observed to increase up to 6 m/s (Fig. 6c). High speed videos reveal that the rise in the velocity corresponds to a jet formation that squeezes the microbubble to form a neck and eventually leads to fragmentation.

Postema et. al[65] in a numerical investigation reported that microbubble fragmentation occurs "if only if" the kinetic energy of the oscillating microbubble becomes higher than the surface energy of the gas liquid interface. Peng et al. 2020[66] report a numerical study of fragmentation of a bubble surrounded by rigid walls in the presence of ultrasound. The fragmentation of microbubbles in presence of ultrasound was simulated using a "three-dimensional lattice Boltzmann pseudopotential model". According to the report, presence of stiff walls has a considerable impact on the evolution process of the bubble under conditions of $\gamma = 0.5$ and $1 \geq \beta \geq 0.71$, where $\gamma = L/H$ and $\beta = R_0/L$ (L is the distance between centre of the bubble to the bottom wall, H is distance between upper and lower wall, R_0 is the initial radius of the bubble). The authors further report that an instantaneous increase in pressure and velocity near the collapse point deforms the bubbles to a dumbbell shape and eventually leads to fragmentation of the bubble. Rigid walls, on the other hand, were reported to have no effect on bubble deformation for smaller values of β ($0.42 \geq \beta \geq 0$) where the bubble stays spherical throughout the process. Therefore, it is clear that the increase in kinetic energy of the fragmenting location during ultrasound exposure than surface energy results into microbubble fragmentation.

No. of microbubble fragments v/s modified capillary no: Fig. 7 presents the plot for the number of microbubble fragments v/s modified capillary number (Ca'). The capillary number (Ca) was modified to include ultrasonic power, so that the influence of ultrasonic power on microbubble characteristics such as microbubble

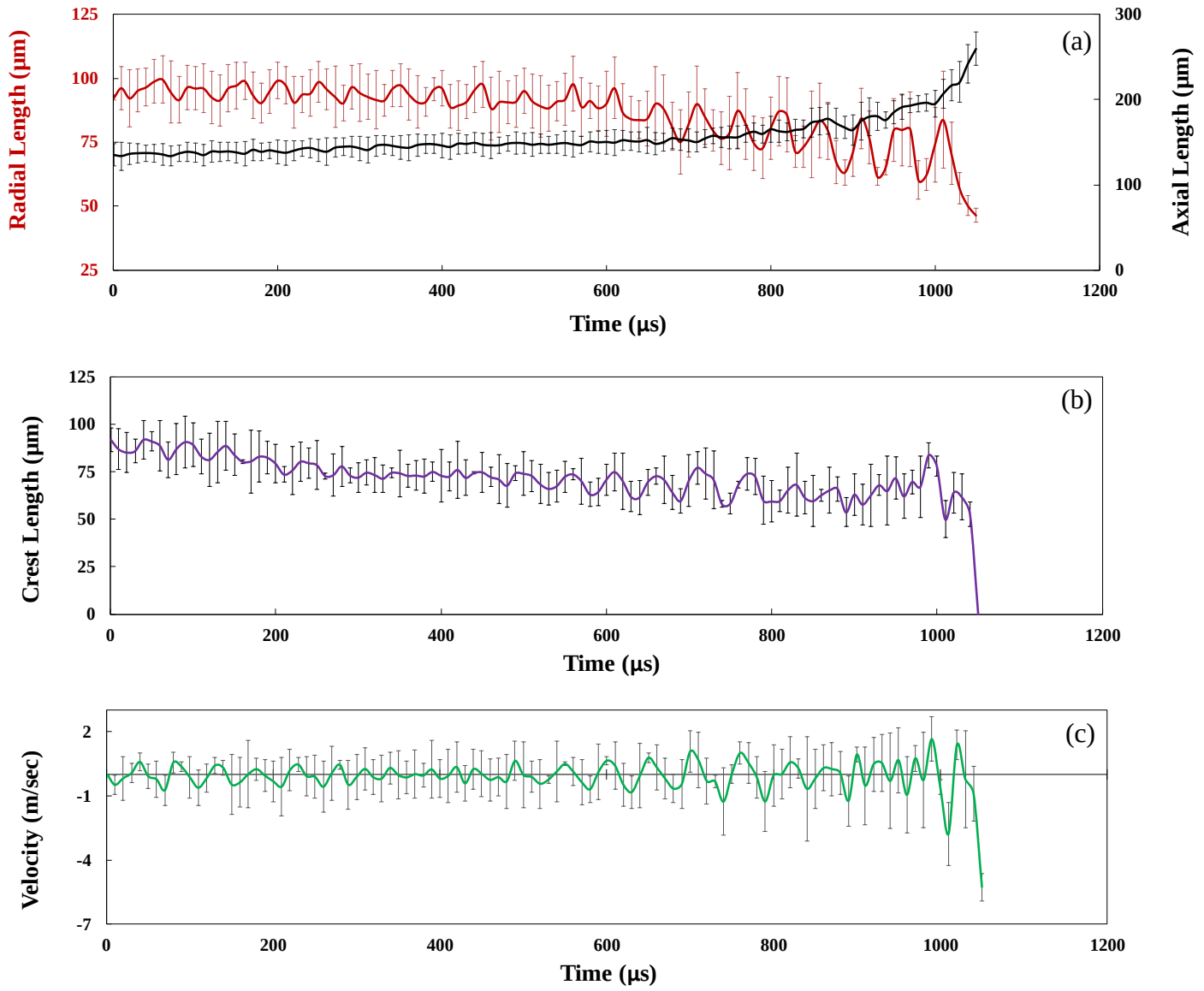

Figure 6. Change in the slug length upon exposure to ultrasound at 20 kHz frequency and 100 % amplitude until first fragmentation. (a) Change in the Radial and the Axial length with reference to the centroid of the gas slug (point 2, marked green in fig. 2) (b) Change in the crest length (point 4, marked red in fig. 2) (c) Velocity profile of the fragmenting point (obtained from video clips) on the microbubble surface traced backwards with time.

size can be easily correlated. Modified capillary no. is defined as $Ca' = \frac{\mu v_g}{\sigma} \times \left[\frac{P}{Pmax}\right]^{1.5}$ where Ca' is the modified capillary no., Ca is the capillary number, μ is the viscosity of the liquid, σ is the surface tension of the gas liquid interface, v_g is the gas velocity, P is the operating power, and P_{max} is the maximum operating power. Microbubbles

of different initial sizes were subjected to fragmentation at four different amplitudes of ultrasound exposure. The total no. of microbubble fragments was calculated by equating the initial and final volumes of the microbubbles, $\frac{\pi}{6}{d_1}^3 = N \times \frac{\pi}{6}{d_2}^3$, where *N* is the fragmentation number which corresponds to the fragmentation of a single microbubble of initial diameter d_1 to *N* identical microbubbles with final diameter d_2. The final size of the microbubble (d_2) is the average size of the microbubble measured using optical particle sizer, Accusizer. It can be observed from Fig. 8 that with an increase in Ca', the total number of microbubble fragments (N) also increases. For a constant viscosity and surface tension of the liquid, an increase in Ca' is controlled by two important parameters (i) velocity of gas (v_g) inside the microfluidic device and (ii) ultrasound power (P) used for microbubble fragmentation. It can be observed that with an increase in Ca', which corresponds to increase in v_g and P, the fragmentation number increases until Ca' reaches to a value of 0.001. However, at higher gas velocities i.e. at high Ca' the total number of fragments become nearly constant (~50000).

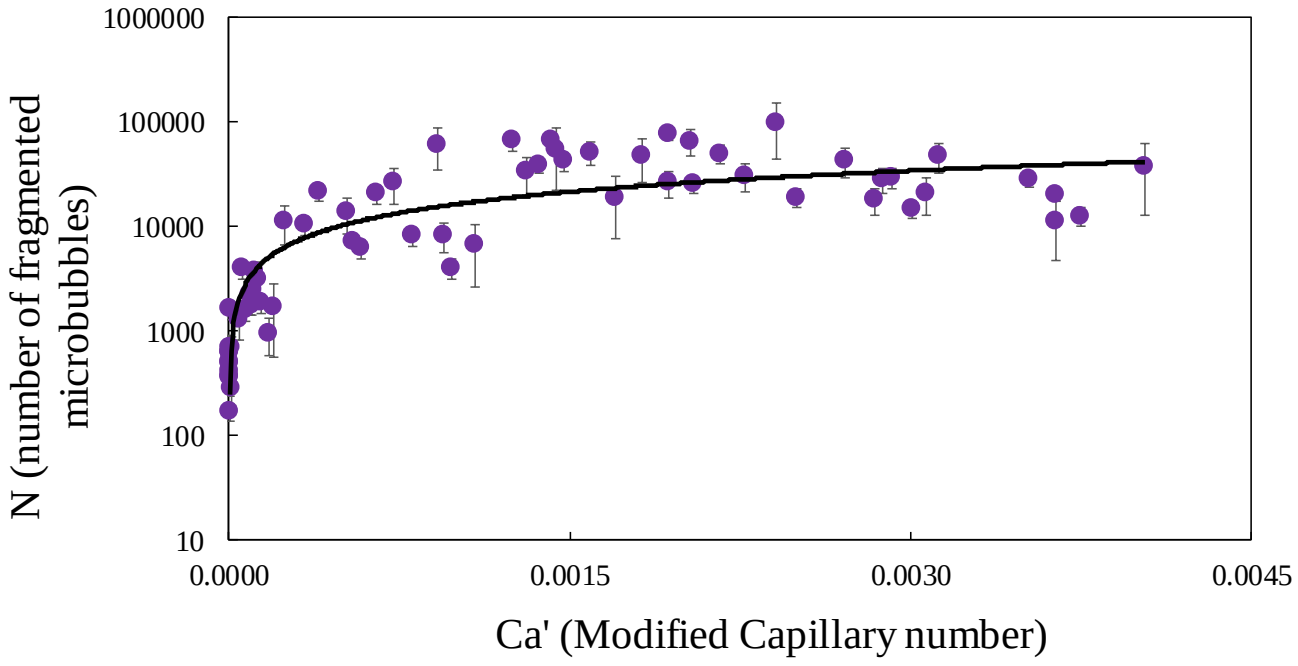

Figure 7. Number of fragmented microbubbles (N) versus modified capillary number

For a microbubble collapsing near a rigid wall, it has been reported that an increase in ultrasonic power increases the velocity of the micro-jet formed during microbubble collapse[57] which leads to quicker and enhanced

fragmentation of the gas slug. Initially, for a very small increase in Ca', N increases considerably. However, after Ca'> 0.001, the higher gas velocity decreases the residence time of the gas slug, hence results in lower ultrasound exposure for each gas slug in a micro-capillary. Therefore, even though the frequency of gas slug coming into a micro-capillary increases with an increase in gas velocity, the fragmentation number does not change significantly

Size isolated microbubbles and their storage stability

Fig. 8 presents size distribution and optical microscopy images of size-sorted microbubbles produced using T-junction combined with ultrasound (Fig. 8a & 8b) and sonication alone followed by centrifugal size isolation (Fig. 8c & 8d). For T-junction combined with ultrasound, microbubbles were collected for 600 s (10 mins) with the sonicator operated for a pulse of 40s ON 20s OFF cycles. The number weighted mean and volume weighted mean of size isolated microbubbles were 1.73 ± 0.2 and 1.76 ± 0.12 µm, respectively and the concentration of the microbubble suspension was found to be ~ $2.8 \pm 1.1 \times 10^9$ bubbles/ ml. The microbubble production rate was found to be ~ $(6.5 \pm 1.2) \times 10^6$ microbubbles/s. On the other hand, the production rate in absence of ultrasound exposure was only ~170 microbubbles/s, and thus about 2000-fold increase in microbubble production rate was observed due to fragmentation process facilitated by ultrasound. The size distribution of fresh microbubble suspension, presented in Fig. 4d, showed peaks between 1-3 µm and 4-7 µm. Size-sorting[26] assisted by centrifugal size isolation for 1 min at 90g, using a sigma laboratory centrifuge (Model no. 136343, made in Germany), allowed separation of small microbubbles (< 1-3 µm) as Infranatant from the microbubble suspension. The size and the concentration of microbubbles stored in aqueous suspensions keep changing with time due to diffusion of gas from the core of the microbubbles to the surrounding medium. Moreover, stability of microbubbles is also affected by polydispersity of microbubble suspension which leads to Ostwald ripening due to the inter-bubble gas exchange[67] and temperature of the microbubble solution, since diffusivity of gas (D_G) is proportional to temperature ($D_G \alpha T^{3/2}$)[22]. Therefore, microbubbles were separated from large bubbles and foam, and stored in vials in air-tight conditions at 4°C.

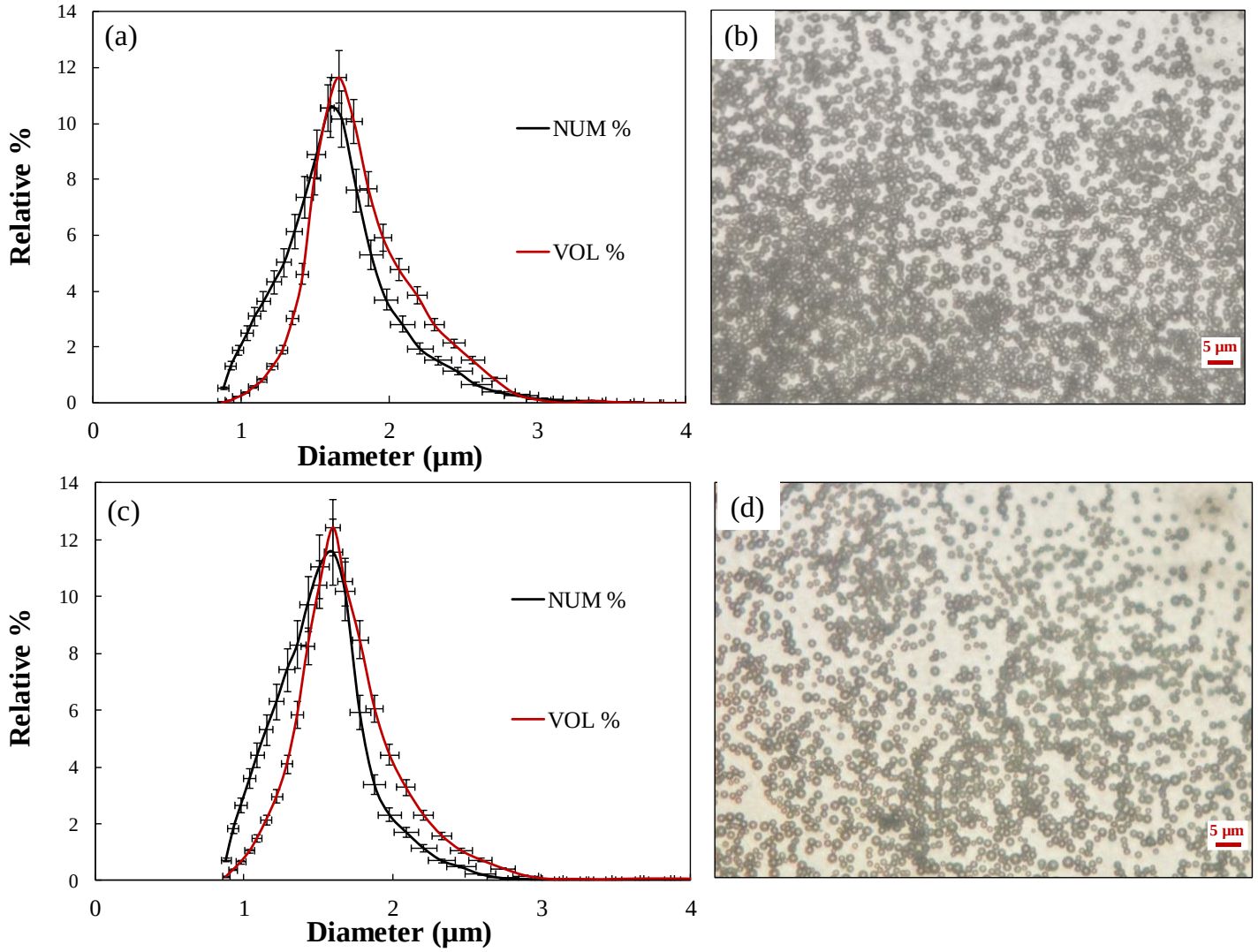

Figure 8. Size distribution of size isolated microbubble suspension produced using (a) microfluidics and sonication combined and (c) sonication alone. Bright field image of the microbubble suspension. (b) microfluidics and sonication combined and (d) sonication alone.

Fig. 8 c & d presents the size distribution and optical images of the size isolated microbubble suspension produced using sonication alone. The freshly prepared microbubble suspension was diluted using DI water and was subjected to centrifugal size isolation to separate microbubbles in the size range of 1-3 µm[26]. It is clear that the size distribution of microbubbles produced using microfluidic combined with ultrasound matches closely with the size distribution of microbubbles produced using sonication alone. This shows that the microfluidic combined

with ultrasound can produce microbubbles in a similar size ranges as that of a traditional technique in a very short span with no exposure of the microbubbles to foreign environment.

The size distribution of the microbubble suspension prepared using T-junction combined with ultrasound was tracked for 30 days. Fig. 9 presents the variation in size distribution with time for size-sorted DSPC-PEG40S shelled SF_6 microbubbles produced at a lipid concentration of 10 mg/mL. Also, Table 2 summarizes the size distribution for a microbubble suspension stored for a period of 30 days.

The concentration of freshly size sorted microbubbles suspension was $2.8 \pm 1.1\times10^9$ bubbles/mL. However, it decreased to $4.5 \pm 0.7\times10^7$ bubbles/mL at the end of 15 days and to $2.3 \pm 1.2\times10^6$ bubbles/mL at the end of 30 days. The number weighted mean size of the microbubbles decreased from 1.73 ± 0.2 µm to 1.45 ± 0.3 µm and the volume weighted mean size decreased from 1.76 ± 0.12 µm to 1.69 ± 0.16 µm over 30 days. It can be observed from Fig. 9 that a new peak start appearing in the size distribution between 0 to 1 µm at 9^{th} day and increases slowly on consecutive days. The absence of any new peaks at higher size ranges and appearance of a new peak at very small size range indicates absence of Ostwald ripening and suggests that the dissolution of microbubbles in the suspension results in appearance of fragments of microbubble shells in a size range of 0 to 1 µm. Thus, decrease in concentration and size of microbubbles, both indicate diffusion of gases from the microbubble core to the surrounding environment as the only mechanism affecting stability of microbubbles in the suspension.

***In-vitro* dissolution of microbubbles in air saturated aqueous environment**

The behaviour of microbubbles in an air saturated environment depends on the shell characteristics, core gas and the air saturation of the aqueous medium. Microbubbles prepared using the acoustic fragmentation process and sonication alone were subjected to dissolution in an air saturated aqueous environment and their dissolution behaviour was observed until complete dissolution. Fig. 10 presents dissolution profiles of 6-8 µm SF_6 microbubbles synthesized using DSPC-PEG40S at lipid concentrations of 2, 5 and 10 mg/mL by sonication alone (Videos S7, S8, and S9) as well using a combination of T-junction & sonication (Videos S10, S11, S12).

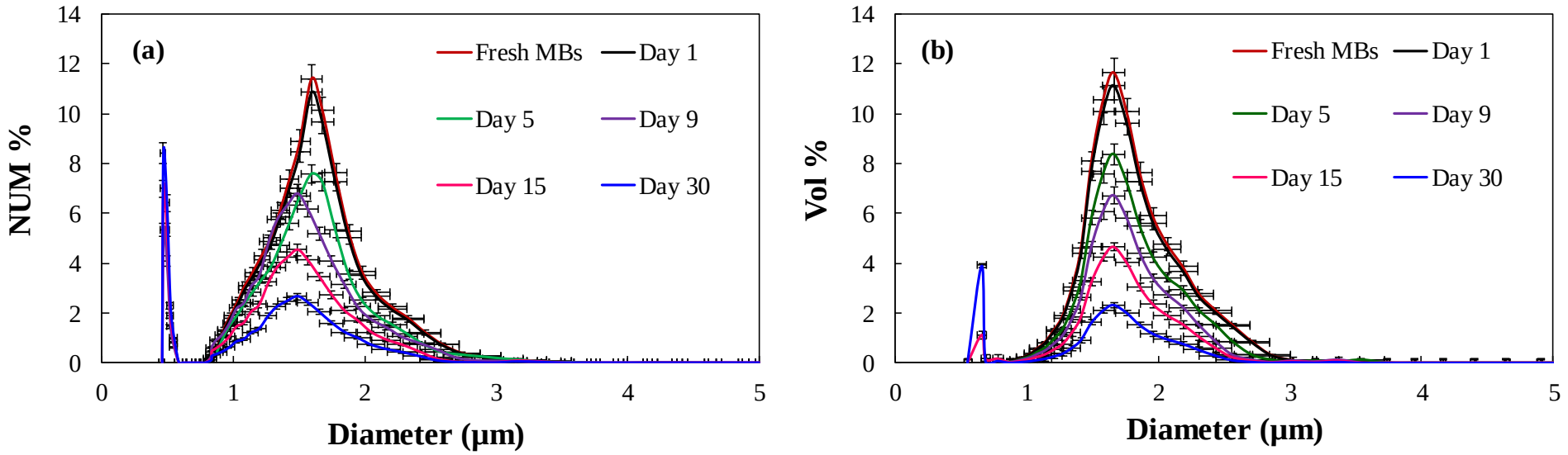

Figure 9. Storage stability of (9:1) molar DSPC-PEG40S containing a concentration of 10 mg/mL shelled microbubbles with SF_6 as the gas core

Table 2. Summary of mean NUM and VOL weighted distribution of microbubbles during storage

		NUM weighted Distribution		VOL weighted Distribution	
Time	**Concentration (microbubbles/ml)**	**Mean(µm)**	**Median (µm)**	**Mean(µm)**	**Median (µm)**
Fresh Microbubbles	$2.8 \pm 1.1\times10^{9}$	1.73 ± 0.2	1.82 ± 0.14	1.76 ± 0.12	1.72 ± 0.11
Day 1	$2.2 \pm 0.8\times10^{9}$	1.76 ± 0.5	1.84 ± 0.2	1.74 ± 0.2	1.71 ± 0.14
Day 5	$4.3 \pm 1.5\times10^{8}$	1.56 ± 0.2	1.54 ± 0.1	1.73 ± 0.16	1.78 ± 0.07
Day 10	$1.4 \pm 1.3\times10^{8}$	1.51 ± 0.1	1.56 ± 0.3	1.77 ± 0.2	1.72± 0.05
Day 15	$4.5 \pm 0.6\times10^{7}$	1.47± 0.2	1.46 ± 0.15	1.64 ± 0.06	1.69 ± 0.11
Day 30	$2.3 \pm 1.2\times10^{6}$	1.45± 0.3	1.43 ± 0.2	1.69 ± 0.16	1.64 ± 0.12

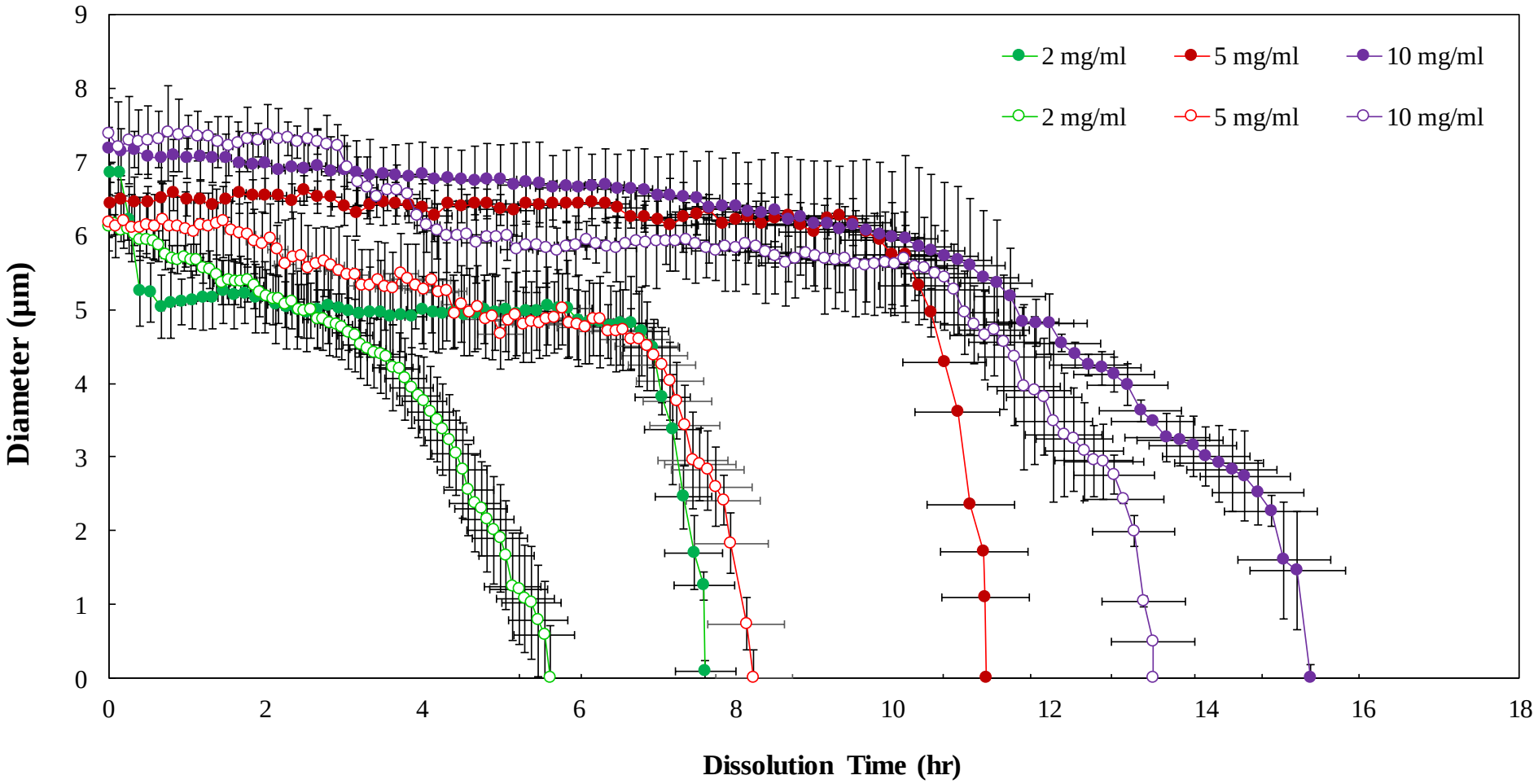

Figure 10. Dissolution profile of 2, 5 & 10 mg/mL DSPC-PEG40S shelled SF_6 microbubbles dissolving in an air saturated environment prepared using microfluidics & sonication combined (unfilled markers) and sonication alone (filled marker).

Microbubbles produced using sonication alone exhibit higher dissolution times than the microbubbles produced using a combination of microfluidics and sonication. Fig. 10 also shows that with an increase in DSPC concentration from 2 to 10 mg/mL, *in-vitro* dissolution time increased from ~ 8 hr to ~15 hr for microbubbles prepared using sonication alone and from ~6 hr to ~13 hr for microbubbles produced using T-junction & sonication combined. Increase in lipid concentration possibly leads to an increase in the number of lipid molecules adsorbed at the gas-liquid interface resulting in higher resistance to gas diffusion and hence increased dissolution times.

Typically, a dissolution process of lipid microbubbles exhibits two phases, a stagnation phase, consisting of minimal change in microbubble size and a shrinkage phase followed by restabilization. In the shrinkage phase the microbubble reduces in size due to shedding of excess lipid molecules, followed by restabilization at a constant diameter which is referred as the "self-healing" property of lipid encapsulation[39]. Dissolution of microbubble produced using low concentration, 2 mg/ml, was observed to follow a more typical dissolution profile.

As the microbubble reduced in size, the microbubbles retained their circular shape due to shedding of lipid molecules from the microbubble shell in a "quasi-continuous" manner[68]. However, with an increase in lipid concentration to 5 and 10 mg/ml, the dissolution time of microbubble was observed to increase, possibly due to higher shell resistance for gas exchange. Abou-saleh et.al[68] observed similar behavior for DPPC shelled microbubbles for varying glycerol concentrations (0-30 % v/v). The authors observed that, for 30 % v/v glycerol concentrations, the microbubbles exhibit a slow dissolution phase where the microbubbles adopted non-spherical and wrinkled shapes during dissolution. The observed behaviour was attributed to the stiffening of the microbubble shell due to higher glycerol concentrations. Accordingly, in this work also, for microbubble produced using 10 mg/ml lipid solution, the dissolution of microbubbles during the initial phase was slower than those produced using 2 and 5 mg/ml lipid concentrations. Finally, microbubbles prepared using T-junction & sonication combined were observed to dissolve completely in ~ 13 hr possibly due to continuous ejection of lipid

molecules from the microbubbles shell. For microbubbles prepared using sonication alone, the microbubbles were observed to be stable upto ~ 15 hr.

Table 3. Comparison of different microfluidic devices for size, production rate and stability

Microfluidic Type	Size (µm)	Production Rate (bubbles/s)	Stability	Ref.
Flow focusing	4.5-20.5	$(0.022\text{-}4) \times 10^5$	-	[69]
Flow focusing	10-20	$(1\text{-}6) \times 10^5$	~ Dissolution time of ~1 min	[70]
Flow focusing	2-10	10^4 - 10^5	~ Dissolution time of 20 hour	[27]
Flow focusing	1-4	10^6	~ Dissolution time of 1 hour	[68]
T-junction	1-2	2×10^6	Concentration of microbubble suspension decreased to 50% in 20 mins	[30]
Two T-junctions in parallel	1-3	$(4.5\text{-}6.6) \times 10^6$	Concentration of microbubble suspension decreased to 50% in 3 days* Dissolution time of ~ 15 hour	This work

* Storage stability was conducted for 30 days.

The longer dissolution time and stagnation phase of microbubbles during dissolution for microbubbles produced using sonication alone and T-junction & sonication combined at higher concentration (5 and 10 mg/ml) can be attributed to acoustic microstreaming[71, 72]. Microstreaming causes local fluid circulation which possibly leads to crowding of lipid molecules at the gas-liquid interface leading to higher mass transfer resistance for gas diffusion. Table 3 presents a comparison of production rates and stability with prior microfluidic systems used for the production of microbubbles. Segers et.al[27] report long term dissolution stability of "Definity-like" PFB core microbubbles in an air saturated environment. The authors observed that PFB core microbubble were stable upto ~ 20 hr and the microbubble reduced to the equilibrium size of ~1 µm for lipid shelled microbubbles. The order of the dissolution time for DSPC shelled SF_6 microbubbles in this work matches closely with the report by Segers et.al. It can be observed from Table 3 that the production rates of the two T-junction microfluidic devices operated in parallel in presence of ultrasound has ~ 2 - 10 times higher production rates of ~ $4.5\text{-}6.6 \times 10^6$ microbubbles/s,

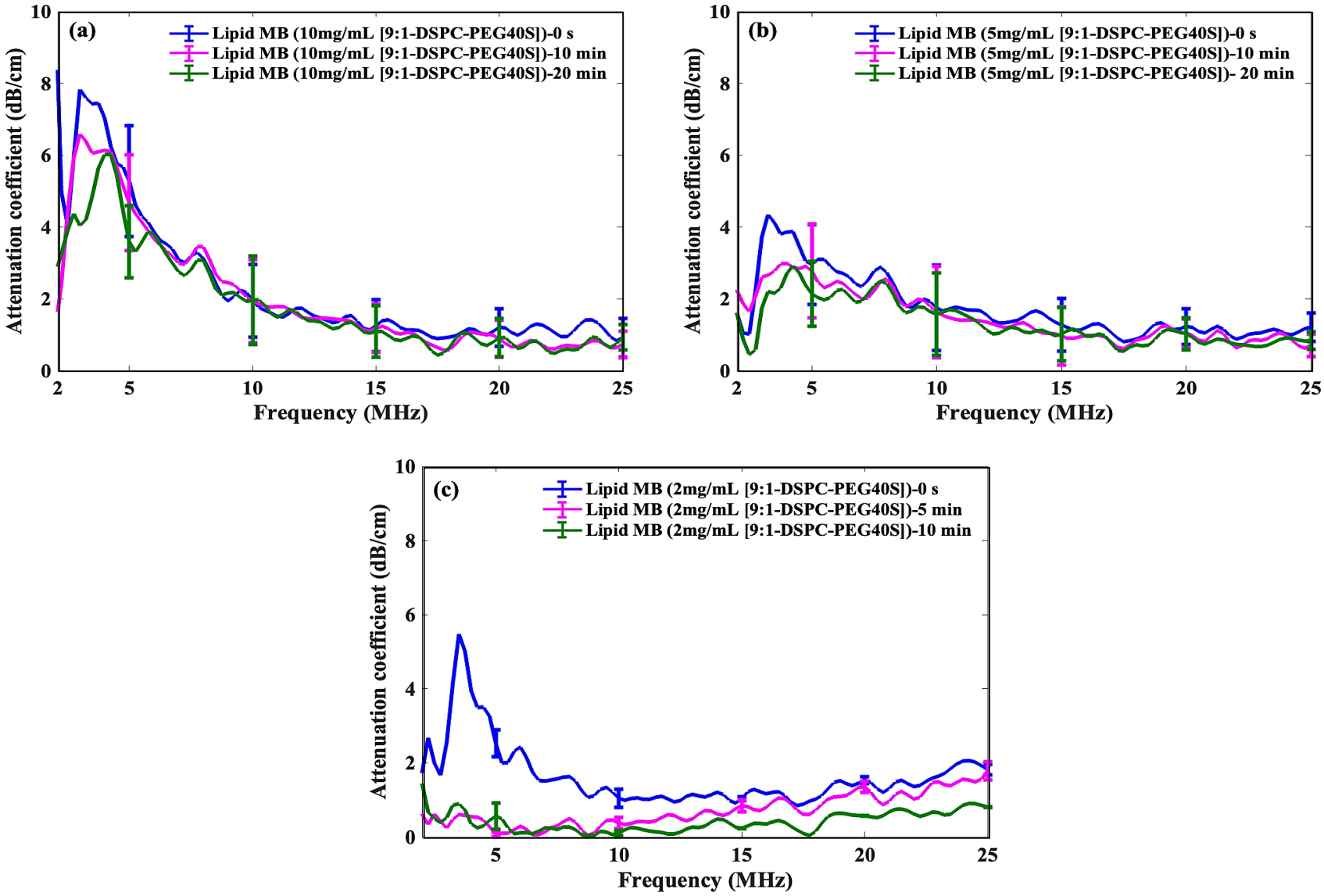

Figure. 11 Experimental attenuation spectrum of DSPC-PEG40S microbubbles with respect to time. (a) 10 mg/mL (b) 5mg/mL (c) 2 mg/mL

compared to earlier reports. This shows that the microfluidic parallelization has enabled easy scale-up of microbubble production in presence of ultrasound.

Broadband attenuation and B-mode imaging

Fig. 11 (a-c) presents the attenuation spectrum of microbubbles for three different DSPC-PEG40S concentration (2, 5 and 10 mg/ml). It can be observed that the attenuation coefficient for microbubbles produced using all DSPC-PEG40S concentration studied in this work peaked between 3-4 MHz frequency. Microbubbles prepared using 10 mg/ml DSPC-PEG40S concentration exhibited approximately twice the attenuation coefficient value at resonance frequency than microbubbles prepared using 5 mg/ml DSPC-PEG40S concentration [Fig. 11 (a-b)].

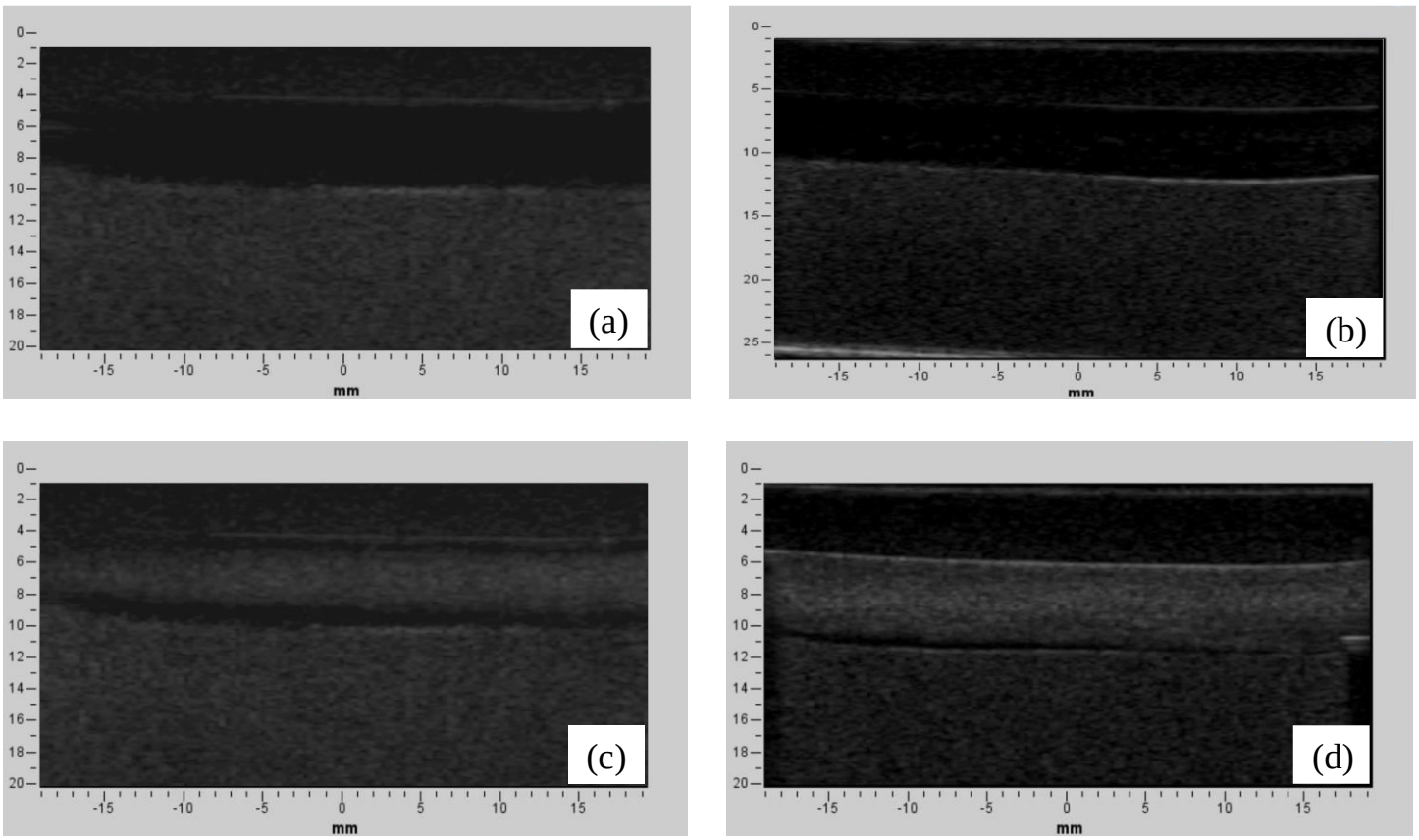

Figure 12. (a-d) Snapshots of B-mode imaging for microbubbles produced using 10 mg/ml DSPC-PEG40S concentration. (a) No microbubbles (b) 10^5 microbubbles/ml (c) 10^6 microbubbles/ml (d) 10^7 microbubbles/ml

At the resonance frequency (3-4 MHz) the attenuation coefficient dropped to 18% and 38% for 10 mg/ml and 5 mg/ml microbubble formulation, respectively within 10 minutes. However, for next 10 minutes, the attenuation coefficient was nearly constant. Moreover, no significant change in the attenuation coefficient value was observed at higher frequencies (10-25 MHz). The stability of microbubbles prepared using 2 mg/ml DSPC-PEG40S concentration was relatively lower.

The attenuation coefficient became nearly zero at the resonance frequency (3-4 MHz) within 5 mins. Fig. S9 (a & b) presents the fitting of experimental (measured) and modelled (estimated) attenuation coefficient as a function of frequency for microbubble prepared using 10 mg/ml and 5 mg/ml DSPC-PEG40S concentrations, respectively. Shell properties of the microbubble suspension produced using 2 mg/ml DSPC-PEG40S concentration was not evaluated since the microbubble suspension was not stable. The size distributions used in shell property assessment were measured as described previously[73].

The measured attenuation coefficients are in agreement with the theoretical fits of the attenuation coefficients with $R^2 > 0.85$. The numerical value of S_P, and S_f were found to be 0.70 N/m, 0.50 $x10^{-6}$ kg/s and 0.65 N/m, 0.48 $x10^{-6}$ kg/s for 5 mg/ml and 10 mg/ml microbubble formulation, respectively. The values of the shell parameter suggest that both the microbubble formulations have similar shell characteristics. The observations are consistent with the report of Guo et.al 2013,[74] where the authors show that the physical properties of the shell are independent of the concentration of the shell material in the solution. The resonance frequency of these microbubble formulations were found to be in the similar range as that of SonoVue microbubble suspensions (3-4 MHz). Moreover, the estimated parameters (S_P = 0.65- 0.70 N/m S_f = 0.48 – 0.50 $x10^{-6}$ kg/s) are comparable with those for commercial formulation Sonovue[74, 75] (S_P = 1.10 N/m, S_f = 0.27 $x10^{-6}$ kg/s).

Fig. 12 presents the snapshots for B-mode imaging for microbubbles prepared at using 10 mg/ml lipid solution. It can be observed that with an increase in the microbubble concentration from 10^5 to 10^7 microbubbles/ml the contrast of the ultrasound image increase. Table 4 presents the CTR and CNR values for microbubble formulation at different concentrations. CTR and CNR characterize the enhancement in contrast by the microbubble

suspension relative to the surrounding tissue. B-mode imaging was carried out at three different concentrations 10^5, 10^6, and a higher dosage of 10^7 microbubbles/mL (see video S13-S18). It was observed that the CTR and CNR values increased with the increase of microbubble concentration, which indicates that the microbubbles prepared using microfluidic and sonication have the ability to improve contrast of an ultrasound image.

Table 4. Estimated CTR and CNR Values for microbubble formulation at different concentrations (microbubbles/ml) obtained from flow phantom imaging and shell properties of the microbubble suspension of different formulations obtained by minimizing the sum squared error between the observed and the predicted attenuation coefficient

Microbubble formulation	Parameter	Concentration (microbubbles/ml)		
		10^5	10^6	10^7
Microbubbles produced using 10 mg/ml DSPC-PEG40S solution	CTR	8.1 ± 1.4	23.1 ± 1.2	29.5 ± 1.2
	CNR	8.8 ± 2.3	24.6 ± 0.8	33.2 ± 1
	S_p (N/m)		0.65	
	S_f (kg/s)		0.48×10^{-6}	
Microbubbles produced using 5 mg/ml DSPC-PEG40S solution	CTR	9.3 ± 1.7	24.5 ± 0.4	30.1 ± 0.3
	CNR	10 ± 1.9	26.1 ± 0.1	34 ± 0.6
	S_p (N/m)		0.7	
	S_f (kg/s)		0.5×10^{-6}	

Conclusions

A large scale production of microbubbles in the size range of 1-8 μm was achieved using acoustic fragmentation of gas slug in a parallel T-junction microfluidic devices. Microbubbles formed by microfluidic devices provide the required gas slugs, which under ultrasound exposure undergo cavitation to form narrow sized microbubble suspension. The rate of microbubble production was observed to increase by an order of 10^4 due to fragmentation of microbubbles, from ~170 bubbles/s to $(6.5 \pm 1.2) \times 10^6$ bubble/s. Acoustic microbubble fragmentation process

was observed using high speed camera at 50000 to 100000 frames/s and the recorded videos were processed to plot the change in slug length and surface velocity of a microbubble until the first fragmentation. The gas slug was observed to follow three stages: (i) oscillation, (ii) slug elongation, (iii) fragmentation. Upon exposure to ultrasound, the gas slug elongates in a capillary tube and undergoes shape oscillation with an increasing number of modes. Significant reduction of radial length of the gas slug was observed during fragmentation. Surface velocity of the gas slug was observed to increase upto ~ 6 m/s, which suggests formation of a micro-jets due to inertial fluid effects that pierce the gas slug and fragments it into smaller microbubbles. The main and the daughter gas slugs were observed to undergo further fragmentation due multiple rebounds within the capillary due to continuous exposure to ultrasound. The total number of fragments and the concentration of the microbubble suspension can be controlled by varying the size of the initial gas slug undergoing fragmentation, the ultrasonic power and gas velocity. At higher ultrasonic power, microbubbles were observed to fragment likely due increased cavitation, however at higher velocities of gas slug the fragmentation number of was observed to remain constant likely due to lower residence time of microbubbles in the microfluidic device. Further, two T-junctions were connected in parallel to produce microbubbles of the order of 10^9, and their shelf stability and dissolution stability were tested. The concentration of microbubble suspension was observed to decrease from ~2.81×10^9/mL to ~ 2.3×10^6/mL at the end of 30 days. The dissolution stability of microbubbles produced using T-junction combined with sonication was compared with those produced using sonication alone. Dissolution times of microbubbles produced using sonication alone was found to be slightly higher (~ 15 hrs) than those produced using T-junction combined with sonication (~13 hrs) possibly due to enhanced adsorption of lipid molecules at the gas-liquid interface when sonication alone was used. The shell properties estimated by broadband attenuation spectroscopy were shell friction (S_P)= 0.65 - 0.70 N/m shell friction (S_f) = 0.48 – 0.50 x10^{-6} kg/s, which was comparable with commercial formulation "Sonovue" (S_P = 1.10 N/m, S_f = 0.27 x10^{-6} kg/s). The CTR and CNR values increased with the increase in concentration of the microbubble suspension, which indicated that the DSPC microbubbles were able to improve the contrast of ultrasound images.

Supplementary Information

High-speed video of microbubble fragmentation with the probe sonicator at 4 mm, 0.5 mm away from the micro-capillary (Video S1, S2). High-speed video of microbubble fragmentation in direct proximity of the micro-capillary (Video S3). High-speed video of fragmentation a 110 µm size gas slug (Video S4), 270 µm gas slug (Video S5), 310 µm gas slug (Video S6). Dissolution video of microbubbles in air-saturated environment prepared by sonication alone at 2mg/ml concentration (Video S7), at 5 mg/ml concentration (Video S8), at 10 mg/ml concentration (Video S9). Dissolution video of microbubbles in air-saturated environment prepared by microfluidic & ultrasound combined at 2mg/ml concentration (Video S10), at 5 mg/ml concentration (Video S11), at 10 mg/ml concentration (Video S12). Flow phantom imaging for 5 mg/ml DSPC-PEG40S concentration with dosage of 10^5 microbubbles/ml (Video S13), 10^6 microbubbles/ml (Video S14), 10^7 microbubbles/ml (Video S15). 10 mg/ml DSPC-PEG40S concentration, 10^5 microbubbles/ml (Video S16), 10^6 microbubbles/ml (Video S17), 10^7 microbubbles/ml (Video S18).

Acknowledgements: The authors gratefully acknowledge the funding from UGC-UKIERI Joint Research Programme (UKIERI III) through a grant no. 184-7/2018 (IC). The authors acknowledge the mechanical workshop facility at UCL, Central Instrumentation Facility at IITGN to carry out this work. The authors thank Vishwas Trivedi for providing help with using the Verasonics platform for performing flow phantom experiments. The authors also acknowledge the financial support from Ministry of Human Resources and Development (MHRD), Government of India.

References

1. Borden, M. A.; Longo, M. L., Dissolution behavior of lipid monolayer-coated, air-filled microbubbles: Effect of lipid hydrophobic chain length. *Langmuir* **2002,** *18* (24), 9225-9233.
2. Sirsi, S.; Borden, M., Microbubble Compositions, Properties and Biomedical Applications. *Bubble Sci Eng Technol* **2009,** *1* (1-2), 3-17.
3. Upadhyay, A.; Dalvi, S. V., Microbubble formulations: synthesis, stability, modeling and biomedical applications. *Ultrasound in medicine & biology* **2018**.
4. Upadhyay, A.; Dalvi, S. V.; Gupta, G.; Khanna, N., Effect of PEGylation on performance of protein microbubbles and its comparison with lipid microbubbles. *Materials Science and Engineering: C* **2017,** *71*, 425-430.
5. Upadhyay, A.; Yagnik, B.; Desai, P.; Dalvi, S. V., Microbubble-mediated enhanced delivery of curcumin to cervical cancer cells. *ACS omega* **2018,** *3* (10), 12824-12831.
6. Li, B.; Aid-Launais, R.; Labour, M.-N.; Zenych, A.; Juenet, M.; Choqueux, C.; Ollivier, V.; Couture, O.; Letourneur, D.; Chauvierre, C., Functionalized polymer microbubbles as new molecular ultrasound contrast agent to target P-selectin in thrombus. *Biomaterials* **2019,** *194*, 139-150.
7. Cesur, S.; Cam, M. E.; Sayın, F. S.; Su, S.; Harker, A.; Edirisinghe, M.; Gunduz, O., Metformin-Loaded Polymer-Based Microbubbles/Nanoparticles Generated for the Treatment of Type 2 Diabetes Mellitus. *Langmuir* **2021**.
8. Klibanov, A. L.; Rasche, P. T.; Hughes, M. S.; Wojdyla, J. K.; Galen, K. P.; Wible Jr, J. H.; Brandenburger, G. H., Detection of individual microbubbles of ultrasound contrast agents: imaging of free-floating and targeted bubbles. *Investigative radiology* **2004,** *39* (3), 187-195.
9. Martin, K. H.; Dayton, P. A., Current status and prospects for microbubbles in ultrasound theranostics. *Wiley Interdisciplinary Reviews: Nanomedicine and Nanobiotechnology* **2013,** *5* (4), 329-345.
10. Helbert, A.; Gaud, E.; Segers, T.; Botteron, C.; Frinking, P.; Jeannot, V., Monodisperse versus Polydisperse Ultrasound Contrast Agents: In Vivo Sensitivity and safety in Rat and Pig. *Ultrasound in Medicine & Biology* **2020,** *46* (12), 3339-3352.
11. Stride, E., Physical principles of microbubbles for ultrasound imaging and therapy. *Cerebrovascular Diseases* **2009,** *27* (Suppl. 2), 1-13.
12. Segers, T.; Kruizinga, P.; Kok, M. P.; Lajoinie, G.; De Jong, N.; Versluis, M., Monodisperse versus polydisperse ultrasound contrast agents: Non-linear response, sensitivity, and deep tissue imaging potential. *Ultrasound in medicine & biology* **2018,** *44* (7), 1482-1492.
13. Ferrara, K.; Pollard, R.; Borden, M., Ultrasound microbubble contrast agents: fundamentals and application to gene and drug delivery. *Annu. Rev. Biomed. Eng.* **2007,** *9*, 415-447.
14. Hernot, S.; Klibanov, A. L., Microbubbles in ultrasound-triggered drug and gene delivery. *Advanced drug delivery reviews* **2008,** *60* (10), 1153-1166.
15. Roovers, S.; Segers, T.; Lajoinie, G.; Deprez, J.; Versluis, M.; De Smedt, S. C.; Lentacker, I., The role of ultrasound-driven microbubble dynamics in drug delivery: From microbubble fundamentals to clinical translation. *Langmuir* **2019,** *35* (31), 10173-10191.
16. Kooiman, K.; Vos, H. J.; Versluis, M.; de Jong, N., Acoustic behavior of microbubbles and implications for drug delivery. *Advanced drug delivery reviews* **2014,** *72*, 28-48.
17. Dewitte, H.; Vanderperren, K.; Haers, H.; Stock, E.; Duchateau, L.; Hesta, M.; Saunders, J. H.; De Smedt, S. C.; Lentacker, I., Theranostic mRNA-loaded microbubbles in the lymphatics of dogs: implications for drug delivery. *Theranostics* **2015,** *5* (1), 97.
18. Lentacker, I.; De Cock, I.; Deckers, R.; De Smedt, S.; Moonen, C., Understanding ultrasound induced sonoporation: definitions and underlying mechanisms. *Advanced drug delivery reviews* **2014,** *72*, 49-64.
19. Chang, E. H., An introduction to contrast-enhanced ultrasound for nephrologists. *Nephron* **2018,** *138* (3), 176-185.
20. Mulvana, H.; Browning, R. J.; Luan, Y.; De Jong, N.; Tang, M.-X.; Eckersley, R. J.; Stride, E., Characterization of contrast agent microbubbles for ultrasound imaging and therapy research. *IEEE transactions on ultrasonics, ferroelectrics, and frequency control* **2016,** *64* (1), 232-251.
21. Khan, A.; Dalvi, S. V., Kinetics of Albumin Microbubble Dissolution in Aqueous Medium. *Soft Matter* **2020**.
22. Upadhyay, A.; Dalvi, S. V., Synthesis, characterization and stability of BSA-encapsulated microbubbles. *RSC Advances* **2016,** *6* (18), 15016-15026.

23. Pancholi, K.; Stride, E.; Edirisinghe, M., Generation of microbubbles for diagnostic and therapeutic applications using a novel device. *Journal of drug targeting* **2008,** *16* (6), 494-501.
24. Mahalingam, S.; Raimi-Abraham, B. T.; Craig, D. Q.; Edirisinghe, M., Formation of protein and protein–gold nanoparticle stabilized microbubbles by pressurized gyration. *Langmuir* **2015,** *31* (2), 659-666.
25. Edirisinghe, M.; Dalvi, S., Preface to the microbubbles: exploring gas-liquid interfaces for biomedical applications special issue. ACS Publications: 2019.
26. Feshitan, J. A.; Chen, C. C.; Kwan, J. J.; Borden, M. A., Microbubble size isolation by differential centrifugation. *Journal of Colloid and Interface Science* **2009,** *329* (2), 316-324.
27. Segers, T.; De Rond, L.; De Jong, N.; Borden, M.; Versluis, M., Stability of monodisperse phospholipid-coated microbubbles formed by flow-focusing at high production rates. *Langmuir* **2016,** *32* (16), 3937-3944.
28. Segers, T.; Lohse, D.; Versluis, M.; Frinking, P., Universal equations for the coalescence probability and long-term size stability of phospholipid-coated Monodisperse microbubbles formed by flow focusing. *Langmuir* **2017,** *33* (39), 10329-10339.
29. Dressaire, E.; Sauret, A., Clogging of microfluidic systems. *Soft Matter* **2017,** *13* (1), 37-48.
30. Carugo, D.; Browning, R. J.; Iranmanesh, I.; Messaoudi, W.; Rademeyer, P.; Stride, E., Scaleable production of microbubbles using an ultrasound-modulated microfluidic device. *The Journal of the Acoustical Society of America* **2021,** *150* (2), 1577-1589.
31. Chen, H.; Li, J.; Zhou, W.; Pelan, E. G.; Stoyanov, S. D.; Arnaudov, L. N.; Stone, H. A., Sonication–Microfluidics for Fabrication of Nanoparticle-Stabilized Microbubbles. *Langmuir* **2014,** *30* (15), 4262-4266.
32. Parhizkar, M.; Edirisinghe, M.; Stride, E., Effect of operating conditions and liquid physical properties on the size of monodisperse microbubbles produced in a capillary embedded T-junction device. *Microfluidics and nanofluidics* **2013,** *14* (5), 797-808.
33. Parhizkar, M.; Edirisinghe, M.; Stride, E., The effect of surfactant type and concentration on the size and stability of microbubbles produced in a capillary embedded T-junction device. *Rsc Advances* **2015,** *5* (14), 10751-10762.
34. Jiang, X.; Zhang, Y.; Edirisinghe, M.; Parhizkar, M., Combining microfluidic devices with coarse capillaries to reduce the size of monodisperse microbubbles. *RSC advances* **2016,** *6* (68), 63568-63577.
35. Khan, A. H.; Surwase, S.; Jiang, X.; Edirisinghe, M.; Dalvi, S. V., Enhancing In Vitro Stability of Albumin Microbubbles Produced Using Microfluidic T-Junction Device. *Langmuir* **2021**.
36. Parhizkar, M.; Stride, E.; Edirisinghe, M., Preparation of monodisperse microbubbles using an integrated embedded capillary T-junction with electrohydrodynamic focusing. *Lab on a Chip* **2014,** *14* (14), 2437-2446.
37. Aramide, B.; Kothandaraman, A.; Edirisinghe, M.; Jayasinghe, S. N.; Ventikos, Y., General Computational Methodology for Modeling Electrohydrodynamic Flows: Prediction and Optimization Capability for the Generation of Bubbles and Fibers. *Langmuir* **2019,** *35* (31), 10203-10212.
38. Kothandaraman, A.; Alfadhl, Y.; Qureshi, M.; Edirisinghe, M.; Ventikos, Y., Effect of the Mixing Region Geometry and Collector Distance on Microbubble Formation in a Microfluidic Device Coupled with ac-dc Electric Fields. *Langmuir* **2019,** *35* (31), 10052-10060.
39. Kwan, J. J.; Borden, M. A., Lipid monolayer dilatational mechanics during microbubble gas exchange. *Soft Matter* **2012,** *8* (17), 4756-4766.
40. Poulichet, V.; Huerre, A.; Garbin, V., Shape oscillations of particle-coated bubbles and directional particle expulsion. *Soft matter* **2017,** *13* (1), 125-133.
41. Raymond, J. L.; Haworth, K. J.; Bader, K. B.; Radhakrishnan, K.; Griffin, J. K.; Huang, S.-L.; McPherson, D. D.; Holland, C. K., Broadband attenuation measurements of phospholipid-shelled ultrasound contrast agents. *Ultrasound in medicine & biology* **2014,** *40* (2), 410-421.
42. Marsh, J. N.; Hall, C. S.; Hughes, M. S.; Mobley, J.; Miller, J. G.; Brandenburger, G. H., Broadband through-transmission signal loss measurements of Albunex® suspensions at concentrations approaching in vivo doses. *The Journal of the Acoustical Society of America* **1997,** *101* (2), 1155-1161.
43. Committee, A. T. S., Methods for specifying acoustic properties of tissue mimicking phantoms and objects. *Laurel, MD, USA: American Institute of Ultrasound in Medicine* **1995**.
44. de Jong, N.; Hoff, L.; Skotland, T.; Bom, N., Absorption and scatter of encapsulated gas filled microspheres: theoretical considerations and some measurements. *Ultrasonics* **1992,** *30* (2), 95-103.

45. Marmottant, P.; Van Der Meer, S.; Emmer, M.; Versluis, M.; De Jong, N.; Hilgenfeldt, S.; Lohse, D., A model for large amplitude oscillations of coated bubbles accounting for buckling and rupture. *The Journal of the Acoustical Society of America* **2005,** *118* (6), 3499-3505.
46. Mercado-Shekhar, K. P.; Kleven, R. T.; Rivera, H. A.; Lewis, R.; Karani, K. B.; Vos, H. J.; Abruzzo, T. A.; Haworth, K. J.; Holland, C. K., Effect of clot stiffness on recombinant tissue plasminogen activator lytic susceptibility in vitro. *Ultrasound in medicine & biology* **2018,** *44* (12), 2710-2727.
47. Goertz, D. E.; Frijlink, M. E.; Tempel, D.; Bhagwandas, V.; Gisolf, A.; Krams, R.; de Jong, N.; van der Steen, A. F., Subharmonic contrast intravascular ultrasound for vasa vasorum imaging. *Ultrasound in medicine & biology* **2007,** *33* (12), 1859-1872.
48. Chen, H.; Evangelou, D.; Loskutova, K.; Ghorbani, M.; Grishenkov, D., On the development of a novel contrast pulse sequence for polymer-shelled microbubbles. *IEEE Transactions on Ultrasonics, Ferroelectrics, and Frequency Control* **2020,** *68* (5), 1569-1579.
49. Poulichet, V.; Garbin, V., Ultrafast desorption of colloidal particles from fluid interfaces. *Proceedings of the National Academy of Sciences* **2015,** *112* (19), 5932-5937.
50. Caskey, C. F.; Kruse, D. E.; Dayton, P. A.; Kitano, T. K.; Ferrara, K. W., Microbubble oscillation in tubes with diameters of 12, 25, and 195 microns. *Applied Physics Letters* **2006,** *88* (3), 033902.
51. Thomas, D. H.; Sboros, V.; Emmer, M.; Vos, H.; De Jong, N., Microbubble oscillations in capillary tubes. *IEEE transactions on ultrasonics, ferroelectrics, and frequency control* **2012,** *60* (1), 105-114.
52. Wu, H.; Zheng, H.; Li, Y.; Ohl, C.-D.; Yu, H.; Li, D., Effects of surface tension on the dynamics of a single micro bubble near a rigid wall in an ultrasonic field. *Ultrasonics sonochemistry* **2021,** *78*, 105735.
53. Ohl, S.-W.; Ow, D. S.-W.; Klaseboer, E.; Wong, V. V.; Camattari, A.; Ohl, C.-D., Creation of cavitation activity in a microfluidic device through acoustically driven capillary waves. *Lab on a Chip* **2010,** *10* (14), 1848-1855.
54. Mobadersany, N.; Sarkar, K. In *Collapse and jet formation of ultrasound contrast microbubbles near a membrane for sonoporation*, 10th International Cavitation Symposium, Baltimore, MD, USA. ASME, 2018.
55. Boyd, B.; Becker, S., Numerical modeling of the acoustically driven growth and collapse of a cavitation bubble near a wall. *Physics of Fluids* **2019,** *31* (3), 032102.
56. Wu, H.; Zhou, C.; Pu, Z.; Lai, X.; Yu, H.; Li, D., Experimental investigation on the effects of the standoff distance and the initial radius on the dynamics of a single bubble near a rigid wall in an ultrasonic field. *Ultrasonics sonochemistry* **2020,** *68*, 105197.
57. Wu, H.; Zhou, C.; Pu, Z.; Yu, H.; Li, D., Effect of low-frequency ultrasonic field at different power on the dynamics of a single bubble near a rigid wall. *Ultrasonics sonochemistry* **2019,** *58*, 104704.
58. Brennen, C. E., Fission of collapsing cavitation bubbles. *Journal of Fluid Mechanics* **2002,** *472*, 153-166.
59. Yamamoto, T.; Hatanaka, S.-i.; Komarov, S. V., Fragmentation of cavitation bubble in ultrasound field under small pressure amplitude. *Ultrasonics sonochemistry* **2019,** *58*, 104684.
60. Zhang, Y.; Li, S., The secondary Bjerknes force between two gas bubbles under dual-frequency acoustic excitation. *Ultrasonics sonochemistry* **2016,** *29*, 129-145.
61. Mettin, R.; Akhatov, I.; Parlitz, U.; Ohl, C.; Lauterborn, W., Bjerknes forces between small cavitation bubbles in a strong acoustic field. *Physical review E* **1997,** *56* (3), 2924.
62. Leighton, T., *The acoustic bubble*. Academic press: 2012.
63. Naper, D., Steric stabilisation. *J. Colloid Interface Sci.* **1977,** *58* (2), 391-400.
64. Lee, J.; Tuziuti, T.; Yasui, K.; Kentish, S.; Grieser, F.; Ashokkumar, M.; Iida, Y., Influence of surface-active solutes on the coalescence, clustering, and fragmentation of acoustic bubbles confined in a microspace. *The Journal of Physical Chemistry C* **2007,** *111* (51), 19015-19023.
65. Postema, M.; Schmitz, G. In *Ultrasonic fragmentation of microbubbles: a theoretical approach of the flash in flash-echo*, 2005 IEEE Engineering in Medicine and Biology 27th Annual Conference, IEEE: 2006; pp 4023-4026.
66. Peng, H.; He, X.; Zhang, J.; Wang, Y., Cavitation bubble collapse between parallel rigid walls with the three-dimensional multi-relaxation time pseudopotential lattice Boltzmann method. *AIP Advances* **2020,** *10* (10), 105104.
67. Sridhar, S.; Patel, A.; Dalvi, S. V., Estimation of storage stability of aqueous microbubble suspensions. *Colloids and Surfaces A: Physicochemical and Engineering Aspects* **2016,** *489*, 182-190.
68. Abou-Saleh, R. H.; McLaughlan, J. R.; Bushby, R. J.; Johnson, B. R.; Freear, S.; Evans, S. D.; Thomson, N. H., Molecular Effects of Glycerol on Lipid Monolayers at the Gas Liquid Interface: Impact on Microbubble Physical and Mechanical Properties. *Langmuir* **2019,** *35* (31), 10097-10105.

69. Wang, S.; Dhanaliwala, A. H.; Chen, J. L.; Hossack, J. A., Production rate and diameter analysis of spherical monodisperse microbubbles from two-dimensional, expanding-nozzle flow-focusing microfluidic devices. *Biomicrofluidics* **2013,** *7* (1), 014103.
70. Chen, J. L.; Dhanaliwala, A. H.; Dixon, A. J.; Klibanov, A. L.; Hossack, J. A., Synthesis and characterization of transiently stable albumin-coated microbubbles via a flow-focusing microfluidic device. *Ultrasound in medicine & biology* **2014,** *40* (2), 400-409.
71. Liu, X.; Wu, J., Acoustic microstreaming around an isolated encapsulated microbubble. *The Journal of the Acoustical Society of America* **2009,** *125* (3), 1319-1330.
72. Cleve, S.; Guédra, M.; Mauger, C.; Inserra, C.; Blanc-Benon, P., Microstreaming induced by acoustically trapped, non-spherically oscillating microbubbles. *Journal of Fluid Mechanics* **2019,** *875*, 597-621.
73. Shekhar, H.; Smith, N. J.; Raymond, J. L.; Holland, C. K., Effect of temperature on the size distribution, shell properties, and stability of Definity®. *Ultrasound in medicine & biology* **2018,** *44* (2), 434-446.
74. Guo, X.; Li, Q.; Zhang, Z.; Zhang, D.; Tu, J., Investigation on the inertial cavitation threshold and shell properties of commercialized ultrasound contrast agent microbubbles. *The Journal of the Acoustical Society of America* **2013,** *134* (2), 1622-1631.
75. Gorce, J.-M.; Arditi, M.; Schneider, M., Influence of bubble size distribution on the echogenicity of ultrasound contrast agents: A study of SonoVue™. *Investigative radiology* **2000,** *35* (11), 661-671.

Supplementary Information

Combining ultrasound and capillary embedded T-junction microfluidic devices to scale up production of narrow sized microbubbles through acoustic fragmentation

Aaqib H. Khan[#], Xinyue Jiang†, Anuj Kaushik[‡], Hari S. Nair[§], Mohan Edirisinghe†, Karla P. Mercado-Shekhar[§], Himanshu Shekhar[‡], and Sameer V. Dalvi[#]*

Chemical Engineering, Indian Institute of Technology Gandhinagar, Palaj, Gandhinagar - 382355, Gujarat, India

† Department of Mechanical Engineering, University College London (UCL), London WC1E 7JE, U.K.

[‡] Electrical Engineering, Indian Institute of Technology Gandhinagar, Palaj, Gandhinagar - 382355, Gujarat, India

[§] Biological Engineering, Indian Institute of Technology Gandhinagar, Palaj, Gandhinagar - 382355, Gujarat, India

***E-mail: sameervd@iitgn.ac.in; Phone: 091-79-2395 2408**

Number of pages: 9

Number of figures: 9 (S1, S2, S3, S4, S5, S6, S7, S8, S9)

Caption for the Supplementary videos:

High-speed video of microbubble fragmentation with the probe sonicator at 4 mm, 0.5 mm away from the micro-capillary **(Video S1, S2).**

High-speed video of microbubble fragmentation in direct proximity of the micro-capillary **(Video S3).**

High-speed video of fragmentation a 110 µm size gas slug **(Video S4),** 270 µm gas slug **(Video S5),** 310 µm gas slug **(Video S6).**

Dissolution video of microbubbles in air-saturated environment prepared by sonication alone at 2mg/ml concentration **(Video S7),** at 5 mg/ml concentration **(Video S8),** at 10 mg/ml concentration **(Video S9).**

Dissolution video of microbubbles in air-saturated environment prepared by microfluidic & ultrasound combined at 2mg/ml concentration **(Video S10),** at 5 mg/ml concentration **(Video S11),** at 10 mg/ml concentration **(Video S12).**

Flow phantom imaging for 5 mg/ml DSPC-PEG40S concentration with dosage of 10^5 microbubbles/ml **(Video S13),** 10^6 microbubbles/ml **(Video S14),** 10^7 microbubbles/ml **(Video S15).**

Flow phantom imaging for 10 mg/ml DSPC-PEG40S concentration, 10^5 microbubbles/ml **(Video S16),** 10^6 microbubbles/ml **(Video S17)**, 10^7 microbubbles/ml **(Video S18).**

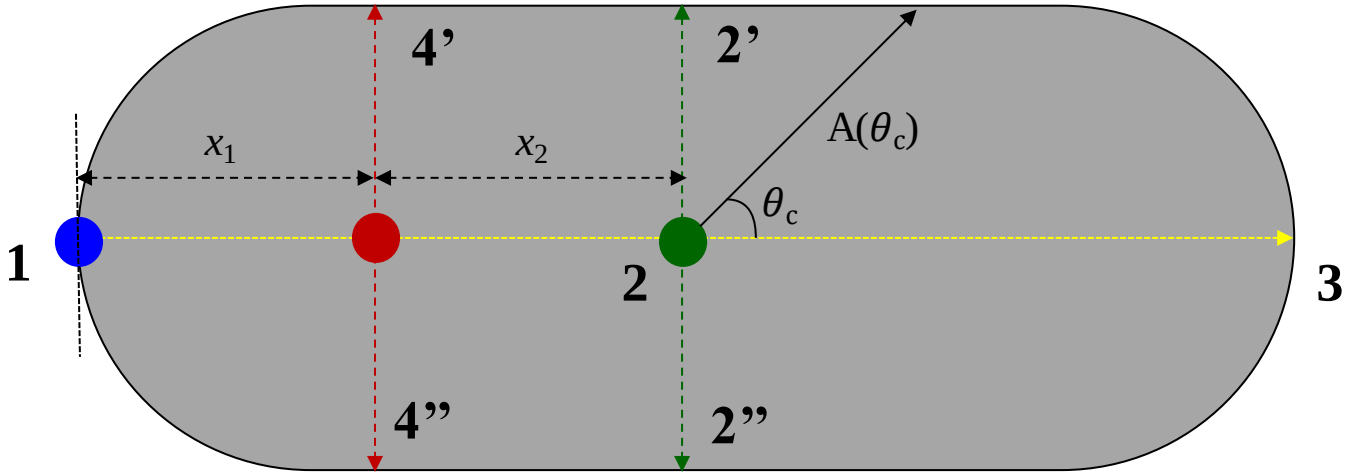

Figure S1. Illustrative gas slug depicting three reference points, centroid of the gas slug (marked as 2) and the farthest point of the gas slug (1 & 3). Red marker illustrates a fragmentation location found using the high speed video clips and back traced keeping the ratio of distance x_1 and x_2 from right farthest point and the centroid constant.

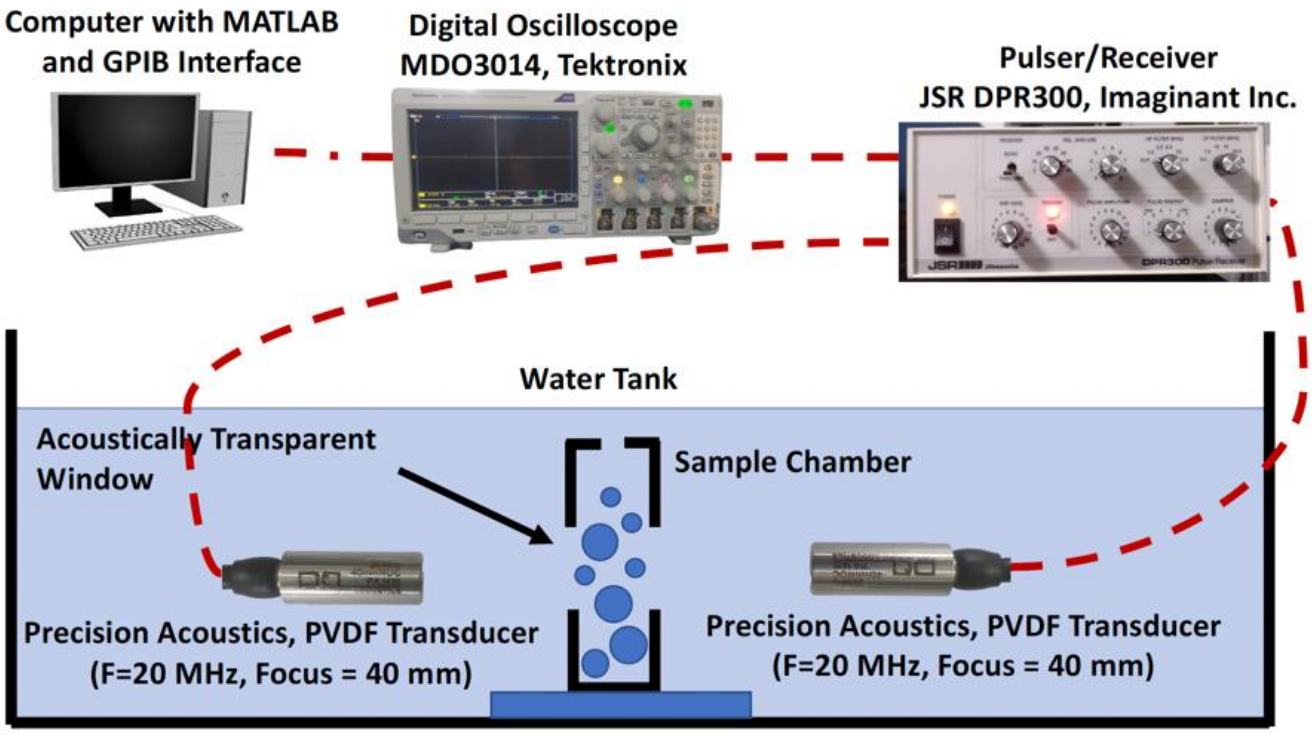

Figure S2. Experimental setup for broadband attenuation spectroscopy measurements

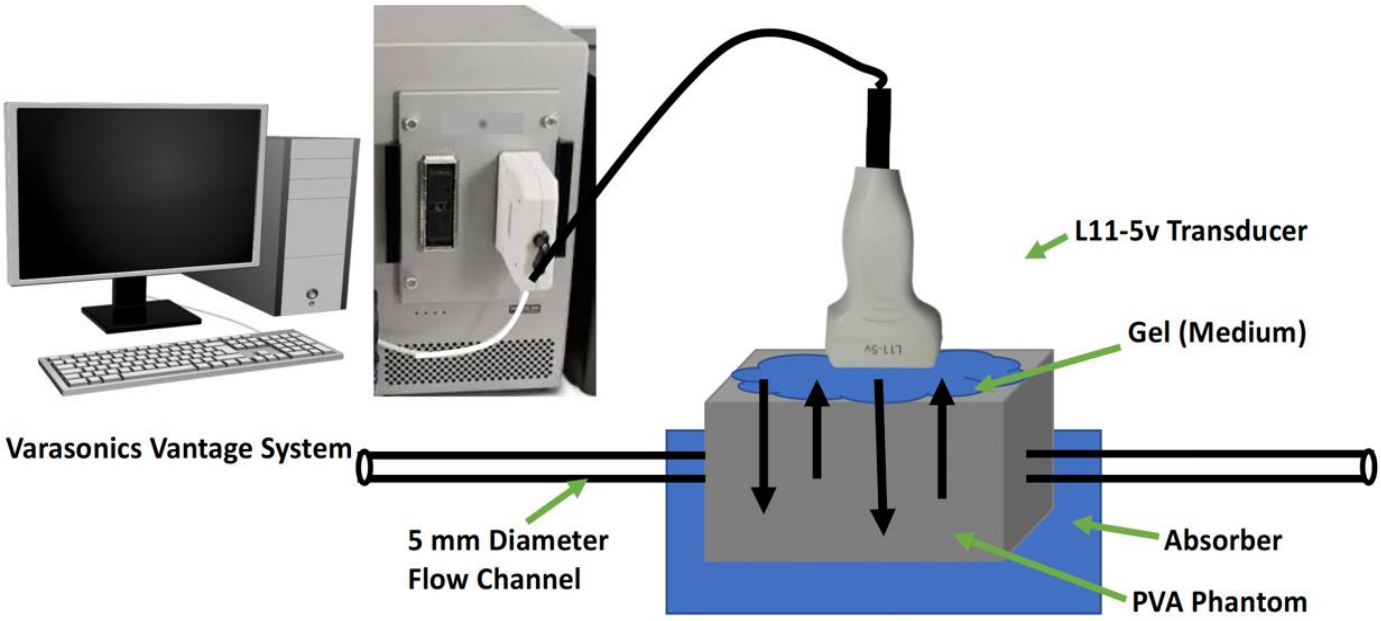

Figure S3. Schematic of experimental setup to characterize the imaging performance of microbubbles by b-mode imaging.

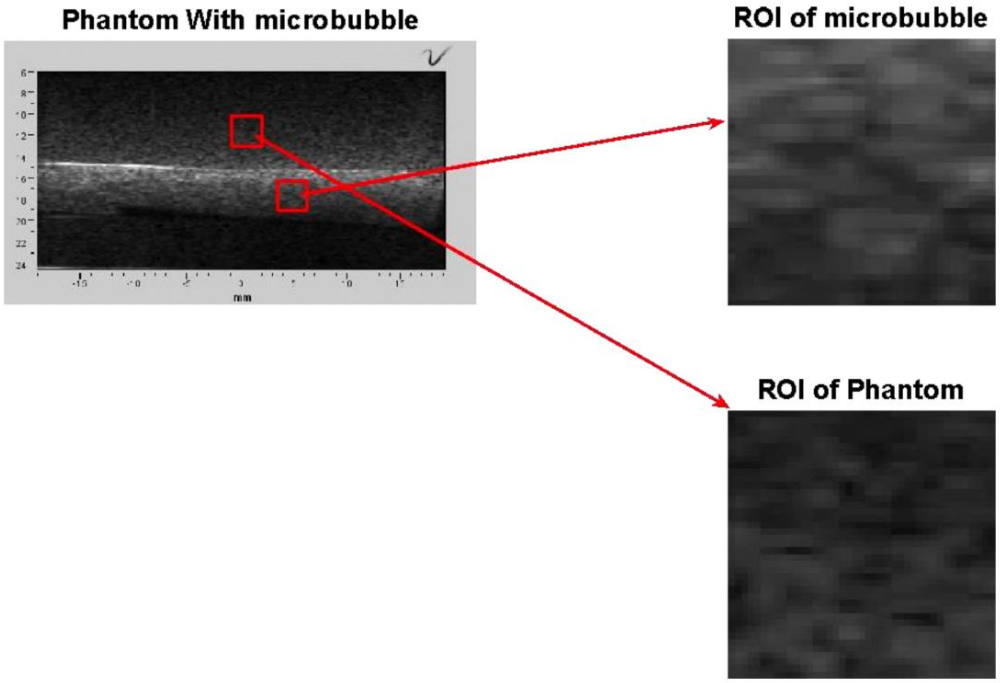

Figure S4. Illustration of region of interest (ROI) selection for the calculation of CTR and CNR values

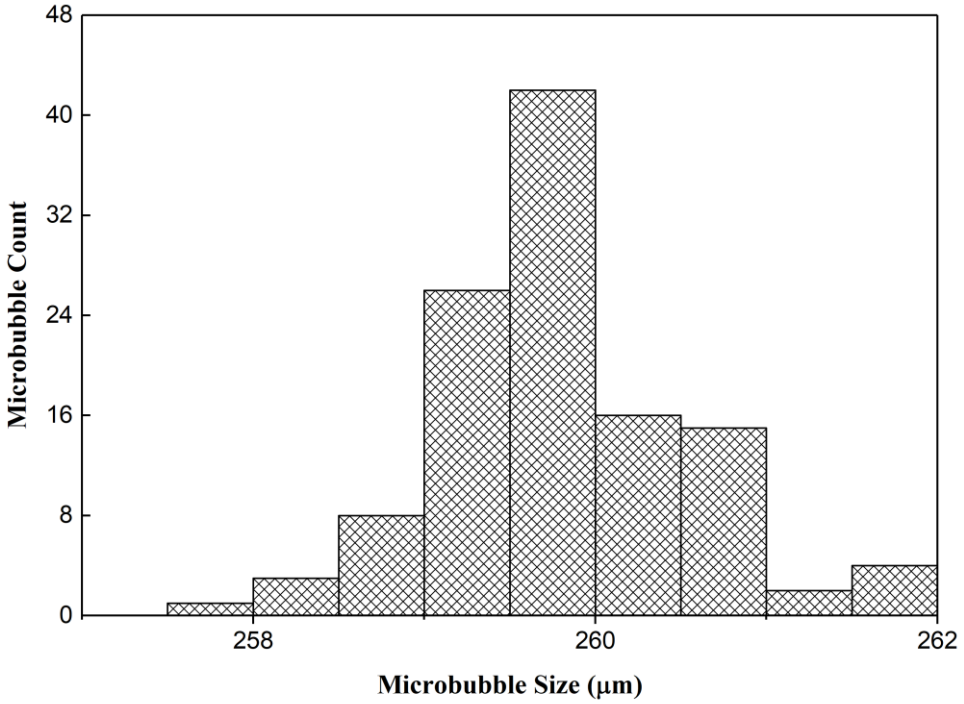

Figure S5. Microbubble size distribution in absence of ultrasound. T-junction with a 200 μm capillary operated at 0.3 ml/min and 0.2 bar pressure

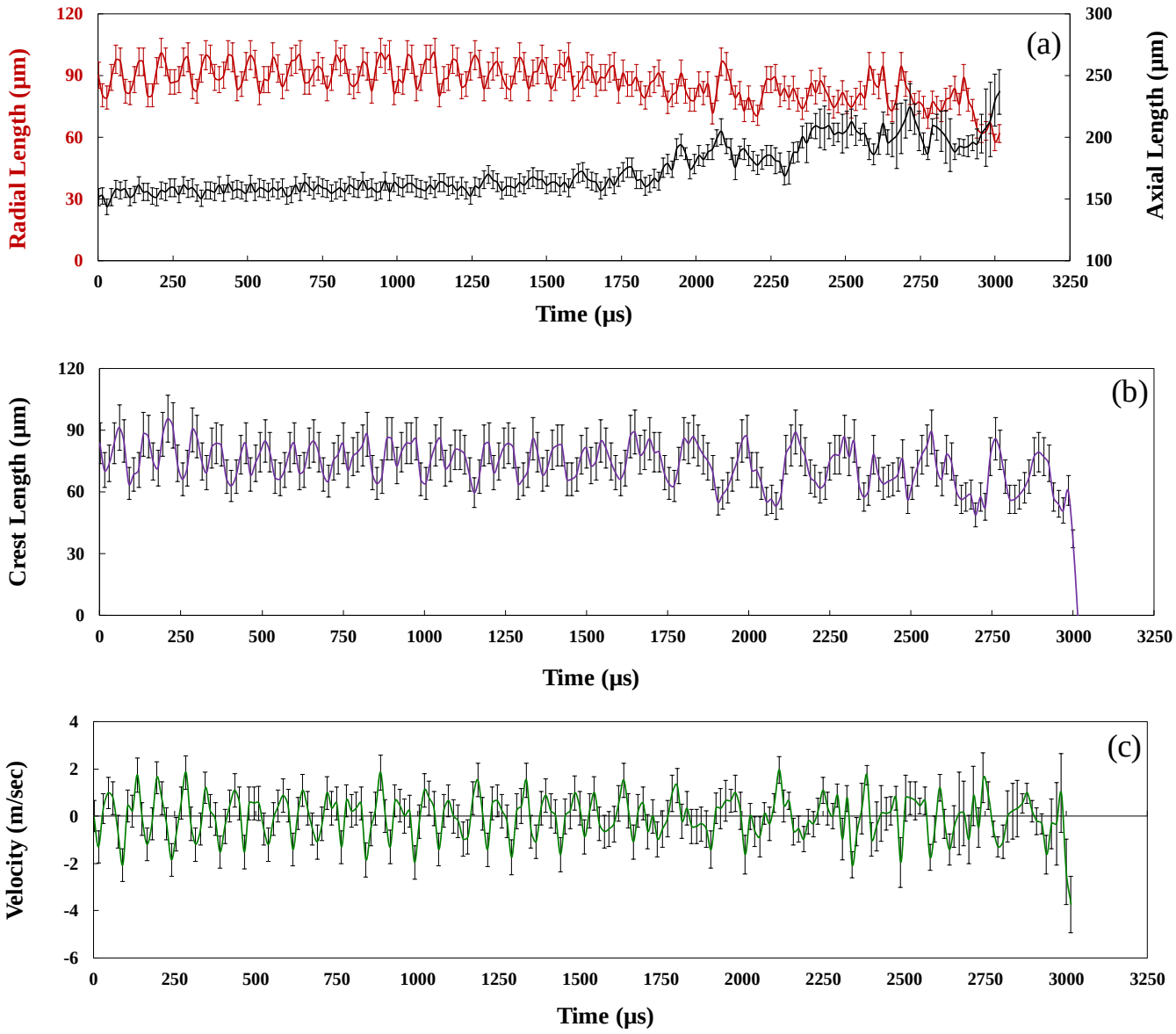

Figure S6. Change in the slug length upon exposure to ultrasound at 20 kHz frequency and 25 % amplitude until first fragmentation. (a) Change in the Radial and the Axial length with reference to the centroid of the gas slug (point 2, marked green in fig. 2) (b) Change in the crest length (point 4, marked red in fig. 2) (c) Velocity profile of the fragmenting point (obtained from video clips) on the microbubble surface traced backwards with time.

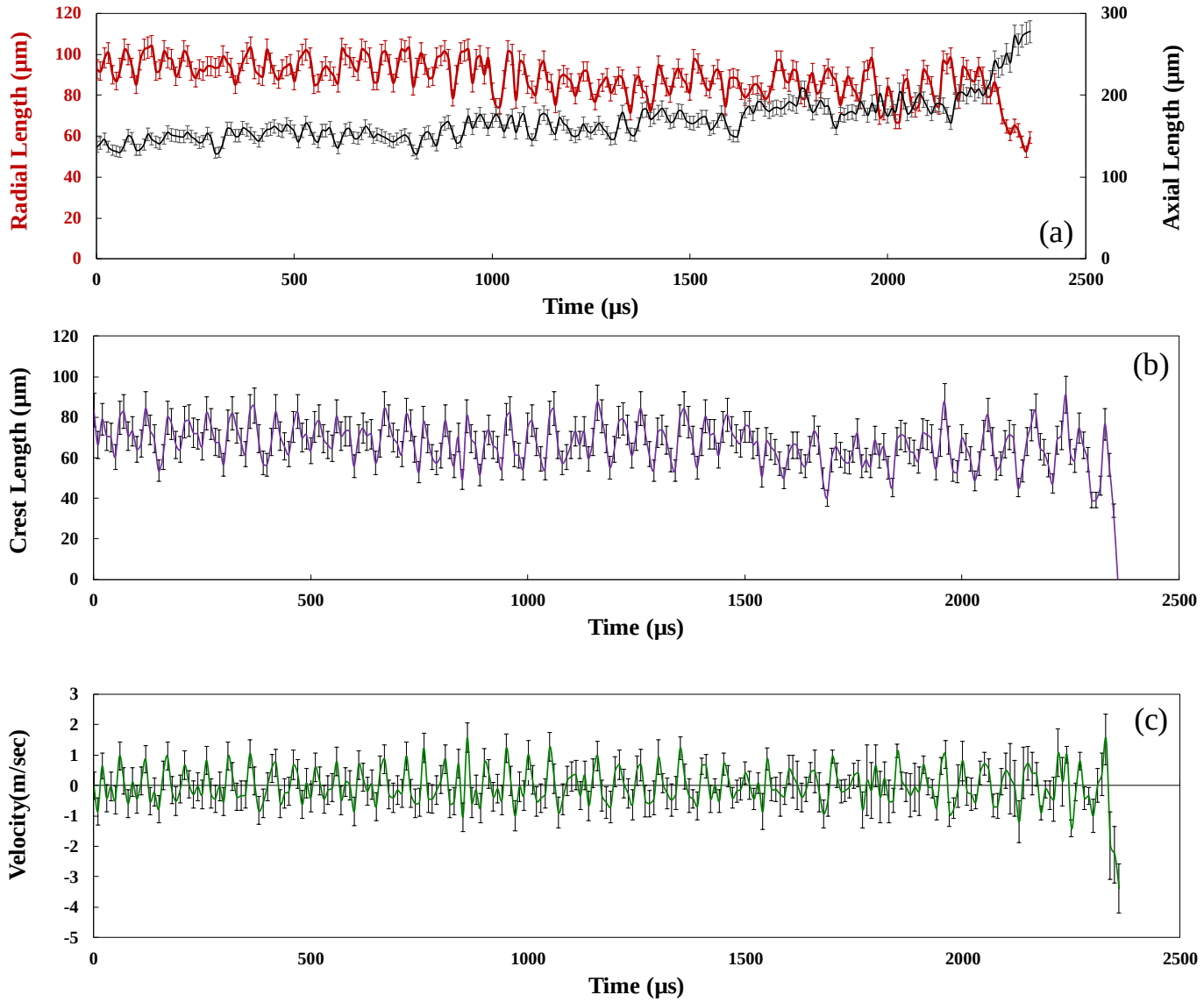

Figure S7. Change in the slug length upon exposure to ultrasound at 20 kHz frequency and 50 % amplitude until first fragmentation. (a) Change in the Radial and the Axial length with reference to the centroid of the gas slug (point 2, marked green in fig. 2) (b) Change in the crest length (point 4, marked red in fig. 2) (c) Velocity profile of the fragmenting point (obtained from video clips) on the microbubble surface traced backwards with time.

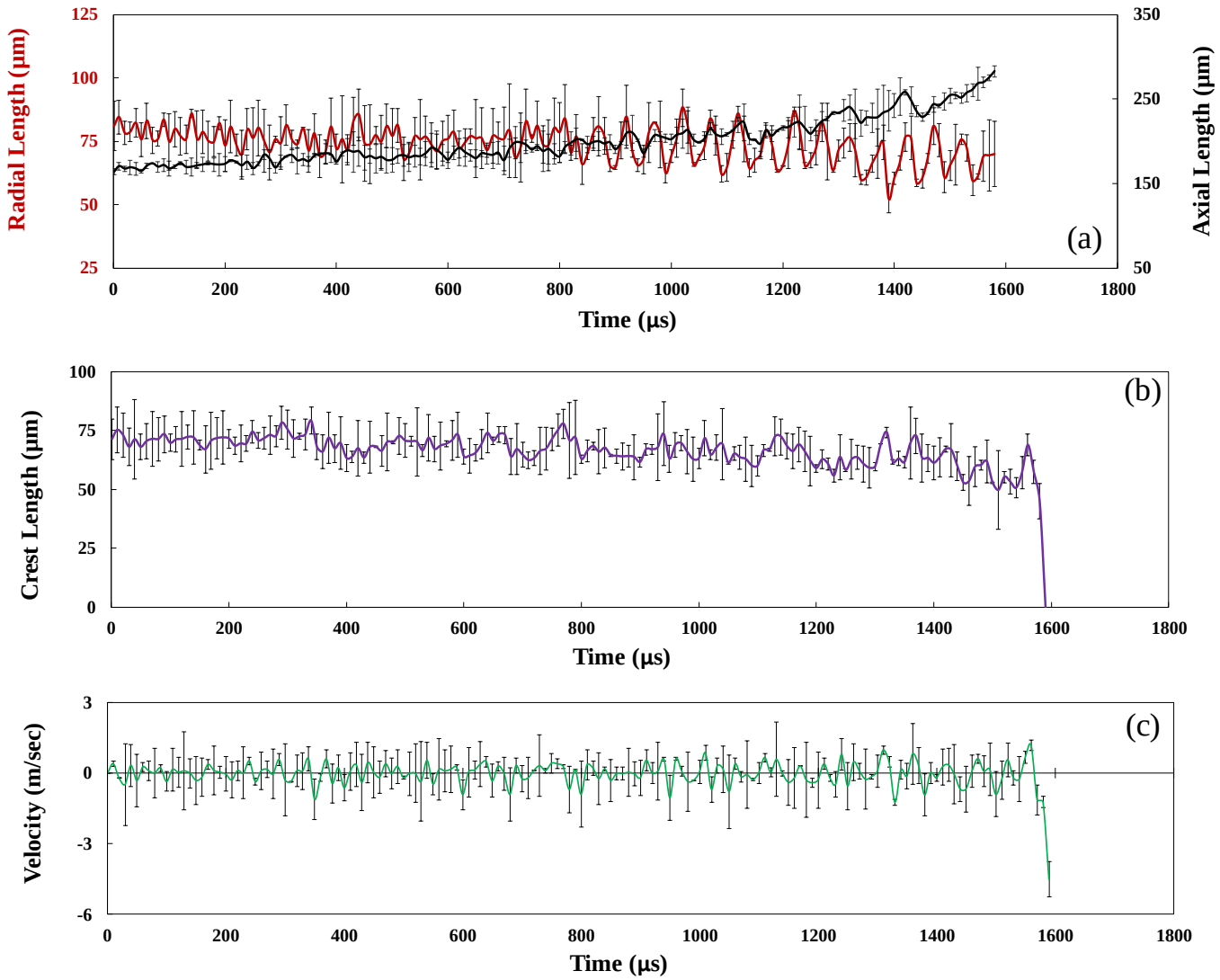

Figure S8. Change in the slug length upon exposure to ultrasound at 20 kHz frequency and 75 % amplitude until first fragmentation. (a) Change in the Radial and the Axial length with reference to the centroid of the gas slug (point 2, marked green in fig. 2) (b) Change in the crest length (point 4, marked red in fig. 2) (c) Velocity profile of the fragmenting point (obtained from video clips) on the microbubble surface traced backwards with time.

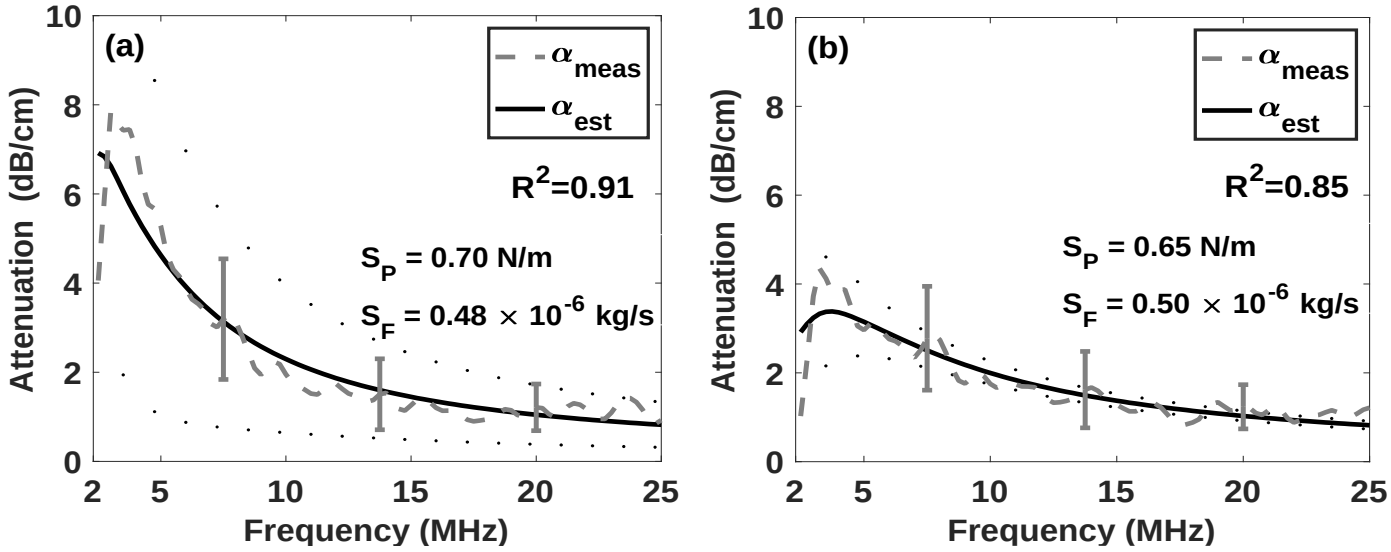

Figure S9. Measured attenuation coefficients as a function of frequency (dashed lines) and theoretical fits (solid lines) for estimation of shell parameters (a) 10 mg/ml, (b) 5 mg/ml DSPC-PEG40S.